



aa/bb/cc/dd-TDI

## **EXPLORING COLD POOL DYNAMICS IN MONAN: INSIGHTS FROM HURRICANES**

Bianca Fusinato

Master's Dissertation from the  
Graduate Program in Meteorology,  
supervised by Dr. Saulo R. Freitas,  
approved on [day] of [month] [year].

URL of the original document:  
<http://urlib.net/xx/yy>

INPE  
São José dos Campos  
2025

**PUBLISHED BY:**

Instituto Nacional de Pesquisas Espaciais - INPE  
Coordenação de Ensino, Pesquisa e Extensão (COEPE)  
Divisão de Biblioteca (DIBIB)  
CEP 12.227-010  
São José dos Campos - SP - Brasil  
Tel.:(012) 3208-6923/7348  
E-mail: pubtc@inpe.br

**BOARD OF PUBLISHING AND PRESERVATION OF INPE INTELLECTUAL PRODUCTION - CEPII (PORTARIA Nº 176/2018/SEI-INPE):**

**Chairperson:**

Dra. Marley Cavalcante de Lima Moscati - Coordenação-Geral de Ciências da Terra (CGCT)

**Members:**

Dra. Ieda Del Arco Sanches - Conselho de Pós-Graduação (CPG)

Dr. Evandro Marconi Rocco - Coordenação-Geral de Engenharia, Tecnologia e Ciência Espaciais (CGCE)

Dr. Rafael Duarte Coelho dos Santos - Coordenação-Geral de Infraestrutura e Pesquisas Aplicadas (CGIP)

Simone Angélica Del Ducca Barbedo - Divisão de Biblioteca (DIBIB)

**DIGITAL LIBRARY:**

Dr. Gerald Jean Francis Banon

Clayton Martins Pereira - Divisão de Biblioteca (DIBIB)

**DOCUMENT REVIEW:**

Simone Angélica Del Ducca Barbedo - Divisão de Biblioteca (DIBIB)

André Luis Dias Fernandes - Divisão de Biblioteca (DIBIB)

**ELECTRONIC EDITING:**

Ivone Martins - Divisão de Biblioteca (DIBIB)

André Luis Dias Fernandes - Divisão de Biblioteca (DIBIB)



aa/bb/cc/dd-TDI

## **EXPLORING COLD POOL DYNAMICS IN MONAN: INSIGHTS FROM HURRICANES**

Bianca Fusinato

Master's Dissertation from the  
Graduate Program in Meteorology,  
supervised by Dr. Saulo R. Freitas,  
approved on [day] of [month] [year].

URL of the original document:  
<http://urlib.net/xx/yy>

INPE  
São José dos Campos  
2025

Cataloging in Publication Data

---

Sobrenome, Nomes.

Cutter      Exploring Cold Pool Dynamics in MONAN: Insights from Hurricanes / Nome Completo do Autor1; Nome Completo do Autor2.  
– São José dos Campos : INPE, 2025.

xx + 78 p. ; (aa/bb/cc/dd-TDI)

Dissertação ou Tese (Mestrado ou Doutorado em Nome do Curso) – Instituto Nacional de Pesquisas Espaciais, São José dos Campos, AAAA.

Orientador : José da Silva.

1. Palavra chave. 2. Palavra chave 3. Palavra chave. 4. Palavra chave. 5. Palavra chave I. Título.

CDU 000.000

---



Esta obra foi licenciada sob uma Licença Creative Commons Atribuição-NãoComercial 3.0 Não Adaptada.

This work is licensed under a Creative Commons Attribution-NonCommercial 3.0 Unported License.

Informar aqui sobre marca registrada (a modificação desta linha deve ser feita no arquivo publicacao.tex).

Informar aqui sobre fontes financiadoras (a modificação desta linha deve ser feita no arquivo publicacao.tex).

**ATENÇÃO! A FOLHA DE  
APROVAÇÃO SERÁ INCLU-  
IDA POSTERIORMENTE.**

Mestrado ou Doutorado em Nome do  
Curso



## **ACKNOWLEDGEMENTS**

acknowledges



## **ABSTRACT**

Structure: GCMs and the need of parameterization, including sub-grid phenomena

Explain about the cold pools and the parameterization

Explain the dissertation's goal: explore this cold pool parameterization and select the best bulk of features to configure the CPTEC model

How are we going to do it?

Since we are working with hurricanes propagating in the ocean, we test other parameterization to take into account - How does it work?

Leave a paragraph to insert the results.

Inside Global Circulation Models (GCMs), precipitation can be modeled through cloud microphysics or convection schemes. Despite advancements in computational capabilities, computational constraints still imply the need for parameterizations for processes not explicitly resolved at the model's grid-scale.

It has been shown that to improve large-scale numerical representation it can be started by improving the sub-grid scale process representation.

Cold Pools correspond to a cold air mass descending within the downdraft. Recent studies show that cold pools are divided into two structures: the cold and dry centers and a moist ring on the edge. When it reaches the surface, it spreads out horizontally, and the high values of moist static energy on the rings combined with the gust front speed can lift the air thermodynamically and mechanically, respectively.

The spatial scale of this phenomenon is translated into sub-grid numerical representations inside the GCMs. It has been shown that cold pools can organize the formation of new convective cells, promoting their aggregation and leading to the development of mesoscale convective systems.

An investigation of the impact of the cold pool parameterization using simulations performed with the Model for Ocean-LaNd-Atmosphere PredictionN (MONAN) is proposed.

Keywords: GCM. Cold Pool. MONAN. Hurricanes. Sea Spray.



**EXPLORANDO A DINÂMICA DE *COLD POOLS* NO MONAN:  
PERSPECTIVAS A PARTIR DE FURACÕES**

**RESUMO**

Traduzir o resumo para português

Palavras-chave: . . . . .



## LIST OF FIGURES

	<u>Page</u>
3.1 MPAS-A meshes and the ability to configure the meshes at different resolutions. . . . .	11
3.2 30km horizontal resolution at native mesh in MONAN. . . . .	12
4.1 Illustration of cross-track and along-track errors. The definitions of Cross-Track Error (CTE) and Along-Track Error (ATE) are based on the distance between an observation (obs) and a forecast (fct) at the same valid time (T). This distance is computed as the great-circle distance. . . . .	17
4.2 Workflow Overview of Hurricane Beryl . . . . .	22
4.3 Workflow Overview of Hurricane Helene . . . . .	24
5.1 2024 Hurricane path according to best track analysis . . . . .	26
5.2 Hurricane Beryl view from the GEOCOLOR composite (left) and Band 13 (right) when passing through the first landfall . . . . .	26
5.3 500 mb Geopotential Height and MSLP at July 8th, 00:00 UTC . . . . .	27
5.4 HB view from NEXRAD (top) and GEOCOLOR composite (bottom) when reaching the Texas Coast. . . . .	28
5.5 Spatial Domain of Hurricane Beryl's Development and Trajectory. . . . .	29
5.6 Comparison of Storm Tracks Across All 15 Experiments . . . . .	32
5.7 Errors (distance) between the trajectories . . . . .	33
5.8 All tracks with selected experiments from Table 5.3 . . . . .	35
5.9 Forecast made for Hurricane Beryl starting at July 3rd (00 UTC), 2024, available at the HAFS website . . . . .	36
5.10 Track errors of the MONAN forecast and ERA5 reanalysis with the best track as reference. 12 hours of model spin-up are withdrawn from the analysis. (a) is displayed the distance error computed as the great circle, and (b), the MAE and RMSE calculated from (a). . . . .	37
5.11 CTE (a) and ATE (b). . . . .	38
5.12 Tracking available by the UK Met Office. . . . .	40
5.13 Overall performance of MONAN trajectory forecasts compared with ERA5 reanalysis. . . . .	41
5.14 Comparison of Forecasted and Observed Central Pressure and Wind Speeds for Hurricane Beryl. Here, a 12-hour model spin-up was also withdrawn, starting the time series on July 3rd, 12 UTC. . . . .	42
5.15 Central Pressure and Maximum Wind Speed Errors. . . . .	43

5.16	Central Pressure and Maximum Wind Speed errors by MONAN compared to ERA5. . . . .	44
5.17	Equitable Threat Score for all experiments, ERA5 dataset and GSMaP dataset. . . . .	45
5.18	Spatially averaged Pearson correlation coefficient over the entire domain	46
5.19	Spatial distribution of daily Pearson correlation values to assess temporal evolution of forecast performance . . . . .	47
5.20	Selected snapshots of rainfall fields from IMERG and GS MaP (30 km resolution) for key time steps . . . . .	54
5.21	Bias relative to GPM-IMERG for tropical cyclone rainfall forecasts . . . . .	55
5.22	Spatial bias relative to GPM-IMERG, highlighting displacement effects in tropical cyclone forecasts . . . . .	56
5.23	Cloud-top brightness temperature snapshots for assessing cloud morphology and vertical structures . . . . .	57
5.24	Effect of horizontal resolution on cloud-top brightness temperature fields	58
5.25	Probability density (left) and cumulative distribution functions (right) of hourly rainfall for each experiment and reference dataset . . . . .	59
5.26	CDFs above the 85th percentile of hourly rainfall, with 95% threshold comparison across datasets . . . . .	60
5.27	CDFs of hourly rainfall at selected time steps within the hurricane domain	61
6.1	Best track trajectory of Hurricane Helene (September 2024) . . . . .	63
6.2	Synoptic-scale interaction between Hurricane Helene and a stationary frontal boundary over the southeastern U.S . . . . .	65
6.3	Satellite images of Hurricane Helene with trailing convection over North Carolina. . . . .	65
6.4	Criar um titulo aqui . . . . .	67

## LIST OF TABLES

	<u>Page</u>
3.1 List of ERA5 Variables Used . . . . .	6
3.3 Physics bulk configuration . . . . .	10
3.4 MONAN Atmospheric Variables Selected for Model Evaluation . . . . .	12
4.1 Metrics used to evaluate rainfall forecast performance . . . . .	19
4.2 Key Research Questions for Track, Intensity, and Rainfall Assessment . .	21
4.3 Key Research Questions for Track, Intensity, and Rainfall Assessment . .	23
5.1 All performed experiments . . . . .	30
5.2 Default values for the cold pool parameterization scheme . . . . .	31
5.3 Selected experiments . . . . .	34
6.1 Highest Rainfall Totals by State . . . . .	66



## **LIST OF ABBREVIATIONS**



## **LIST OF SYMBOLS**



## CONTENTS

	<u>Page</u>
<b>1 INTRODUCTION . . . . .</b>	<b>1</b>
1.1 General objective . . . . .	1
1.2 Specific objectives . . . . .	1
1.3 Scientific questions . . . . .	1
1.4 Thesis organization . . . . .	1
<b>2 LITERATURE REVIEW . . . . .</b>	<b>3</b>
2.1 Overview of convective cloud dynamics . . . . .	3
2.2 Cold pools . . . . .	3
2.3 The mass-flux approach . . . . .	3
2.4 The cold pool parameterization . . . . .	3
2.5 Hurricanes - a model forecast view . . . . .	3
2.6 Key points recall . . . . .	3
<b>3 DATA AND MODEL . . . . .</b>	<b>5</b>
3.1 Data . . . . .	5
3.1.1 IBTrACS . . . . .	5
3.1.2 ERA5 . . . . .	5
3.1.3 GPM-IMERG . . . . .	7
3.1.4 GPM-MERGIR . . . . .	8
3.1.5 GSMAp . . . . .	8
3.2 Numerical model: MONAN . . . . .	9
3.2.1 Initial condition generation . . . . .	13
3.2.2 Post-processing . . . . .	13
<b>4 METHODOLOGY: METRICS AND DIAGNOSTIC FIELDS .</b>	<b>15</b>
4.1 Trajectory . . . . .	15
4.2 Intensity . . . . .	17
4.3 Rainfall . . . . .	18
4.4 Hurricane Beryl workflow . . . . .	20
4.5 Hurricane Helene workflow . . . . .	23
<b>5 CASE STUDY: HURRICANE BERYL . . . . .</b>	<b>25</b>

5.1	Event description - hurricane Beryl . . . . .	25
5.2	Results and analysis of hurricane Beryl . . . . .	29
5.2.1	Trajectory . . . . .	34
5.2.2	Intensity . . . . .	40
5.2.3	Rainfall . . . . .	44
5.2.3.1	Pattern and spatial rainfall distribution . . . . .	44
5.2.3.2	Rainfall mean and overall distribution . . . . .	50
5.2.3.3	Rainfall extremes . . . . .	52
5.2.3.4	MONAN performance at forecasting rainfall . . . . .	53
5.2.4	Discussion of key outcomes . . . . .	53
<b>6</b>	<b>CASE STUDY: HURRICANE HELENE – TESTING THE IMPROVED PARAMETRIZATION . . . . .</b>	<b>63</b>
6.1	Event description - Helene . . . . .	63
6.2	Results and analysis of hurricane Helene . . . . .	68
6.2.1	Trajectory . . . . .	68
6.2.2	Intensity . . . . .	68
6.2.3	Rainfall . . . . .	68
6.2.3.1	Pattern and spatial rainfall distribution . . . . .	68
6.2.3.2	Rainfall mean and overall distribution . . . . .	68
6.2.3.3	MONAN performance at forecasting rainfall . . . . .	68
6.3	Discussion of key outcomes . . . . .	68
<b>7</b>	<b>CONCLUSIONS AND FUTURE WORK . . . . .</b>	<b>69</b>
7.1	Future Work . . . . .	69
<b>A</b>	<b>APPENDIX - THE MASS FLUX DEDUCTION . . . . .</b>	<b>71</b>
<b>A</b>	<b>APPENDIX B - THE TRACKING ALGORITHM . . . . .</b>	<b>73</b>
<b>REFERENCES</b>		<b>75</b>

## 1 INTRODUCTION

### 1.1 General objective

To explore a cold pool parameterization coupled with the Grell-Freitas convection parameterization within the Model for Ocean-laNd-Atmosphere predictioN (MONAN).

### 1.2 Specific objectives

- a) Assess the impact of the cold pool parameterization scheme on hurricane forecasted trajectory, intensity and rainfall;
- b) Perform sensitivity experiments within a hurricane case study, investigating the influence of initial conditions, cold pool duration, the displacement of the maximum mass flux height, type of initial condition and resolution;
- c) Identify the optimal parameter configuration for the cold pool parameterization to be used in MONAN;
- d) Evaluate the performance of this optimal configuration in other hurricane case study.

### 1.3 Scientific questions

This work builds upon the findings and open issues identified in Freitas et al. (2024). The following scientific questions are proposed:

- Does the GF-Cold Pool (GF-CP) scheme improve the forecast of hurricane trajectory, intensity, and rainfall in MONAN?
- Which parameters within the GF-CP have the most significant influence on hurricane representation in MONAN?
- How robust is the optimal GF-CP configuration when applied to a different hurricane event?
- Can improvements in cold pool representation lead to better rainfall predictions in tropical cyclones?

### 1.4 Thesis organization



## **2 LITERATURE REVIEW**

**2.1 Overview of convective cloud dynamics**

**2.2 Cold pools**

**2.3 The mass-flux approach**

**2.4 The cold pool parameterization**

**2.5 Hurricanes - a model forecast view**

**2.6 Key points recall**



## 3 DATA AND MODEL

### 3.1 Data

This section presents the observational datasets used as a reference for evaluating the model forecasts. The selected datasets, described in detail in Sections 3.1.1 to 3.1.5, are commonly employed in tropical cyclone studies and provide reliable information on storm trajectory, intensity, and precipitation. They have been used in several studies (ZHOU; MATYAS, 2021; BOPAPE et al., 2021; DULAC et al., 2024; YANG et al., 2024; MAY et al., 2024) and support a robust assessment of the model’s performance

#### 3.1.1 IBTrACS

The International Best Track Archive for Climate Stewardship (IBTrACS) (KNAPP et al., 2010) offers comprehensive data on the location and intensity of global tropical cyclones. It emphasizes parameters such as geographic position (latitude and longitude), maximum sustained wind speed (measured in knots), and minimum central pressure (in millibars). A complete list of variables and their definitions can be found at the provided link <sup>1</sup>.

This dataset features a spatial resolution of 0.1° (approximately 10 km) and primarily reports data at a temporal resolution of 6 hours, although it can be interpolated to intervals of 3 hours; for our purposes, we will be utilizing the 6-hour data. The dataset covers the period from 1841 to the present, allowing users to explore it by searching for specific oceanic basins, including the North Atlantic, South Atlantic, Eastern North Pacific, Western North Pacific, South Pacific, South Indian, and North Indian.

The dataset is built upon information from various agencies. According to the documentation, the sources of this information include all available resources utilized by forecasters, such as surface observations, aircraft reconnaissance flights, and satellite observations.

#### 3.1.2 ERA5

ERA5 (HERSBACH et al., 2020) represents the fifth generation of atmospheric reanalysis conducted by the European Centre for Medium-Range Weather Forecasts

---

<sup>1</sup><[https://www.ncei.noaa.gov/sites/g/files/anmtlf171/files/2025-04/IBTrACS\\_version4r01\\_Technical\\_Details.pdf](https://www.ncei.noaa.gov/sites/g/files/anmtlf171/files/2025-04/IBTrACS_version4r01_Technical_Details.pdf)>

(ECMWF), serving as a vital resource for both global climate and weather studies. This reanalysis integrates a forecast model with an advanced data assimilation scheme. Specifically, ERA5 employs the ECMWF Integrated Forecast System (IFS) CY41R2 forecast model, executing twice-daily short-term forecasts (18 hours) derived from analyses conducted at 06:00 and 18 UTC. Check the link <sup>2</sup> for a comprehensive understanding of the physical parameters encompassed within the model. The 4D-Var data assimilation method assimilates a diverse array of observations, including satellite data, ground station measurements, instrumented buoy data, and reconnaissance aircraft information. This process utilizes 12-hour time windows from 09 UTC to 21 UTC and from 21 UTC to 09 UTC (the subsequent day).

The initial configuration of the product involves 137 hybrid sigma/pressure levels in the vertical, with the uppermost level being at 0.01 hPa, and it maintains a horizontal resolution of 0.28125° (approximately 30km). Atmospheric data are accessible across interpolated 37 pressure levels. Consequently, the dataset comprises four primary subsets for download: hourly and monthly products, available on pressure levels (restricted to 37 levels) and single levels that encompass atmospheric, ocean-wave, and land surface quantities.

Reanalyses are not constrained by the necessity for timely forecasts, which allows for an extended period to collect observations. Furthermore, when assessing historical data, enhanced versions of the original observations can be integrated, thereby enhancing the quality of the reanalysis product. As a result, reanalyses provide a physically and dynamically consistent global representation of the atmospheric state at each time step. The major advantage of atmospheric reanalysis, particularly in the context of studying tropical cyclones, lies in its capacity to facilitate the analysis of the internal three-dimensional structure of contemporary TCs, alongside the large-scale environmental conditions surrounding them ([DULAC et al., 2024](#)).

The ERA5 data is accessible via the Climate Data Store and downloadable through the Climate Data Store (CDS) Application Program Interface (API). The variables under investigation are highlighted in the table below.

Table 3.1 - List of ERA5 Variables Used

---

<sup>2</sup><<https://www.ecmwf.int/en/elibrary/79697-ifs-documentation-cy41r2-part-iv-physical-processes>>

Variable name	Long name	Unit
msl *	Mean sea level pressure	Pa
i10fg *	Instantaneous 10 metre wind gust	m s <sup>-1</sup>
tp *	Total precipitation	m
sst *	Sea Surface Temperature	K
press **	Pressure	Pa
u **	U component of wind (Zonal Wind)	m s <sup>-1</sup>
v **	V component of wind (Meridional Wind)	m s <sup>-1</sup>

Legend: \* single levels; \*\* pressure levels.

Source: Made by the author (2025).

### 3.1.3 GPM-IMERG

NASA's Integrated Multi-satellite Retrievals for GPM (Global Precipitation Measurement) (IMERG) (HUFFMAN, 2019) algorithm synthesizes information from the GPM satellite constellation. Satellite data are particularly valuable to get information in areas of the Earth where ground-based precipitation-measuring instruments are limited, such as the Atlantic's Main Development Region.

According to the Technical Documentation <sup>3</sup>, estimates from various precipitation-relevant passive microwave (PMW) sensors within the GPM constellation are processed using an algorithm. These estimates are then gridded, intercalibrated with the GPM Combined Radar Radiometer Analysis product, and integrated into half-hourly fields with a horizontal resolution of  $0.1^\circ \times 0.1^\circ$ , covering latitudes from  $60^\circ\text{S}$  to  $60^\circ\text{N}$ . This data is provided to the Climate Prediction Center (CPC) Morphing-Kalman Filter (CMORPH-KF) quasi-Lagrangian time interpolation procedure, as well as undergoing a re-calibration that applies to the Precipitation Estimation from Remotely Sensed Information using Artificial Neural Networks (PERSIANN) Dynamic Infrared–Rain Rate (PDIR) infrared precipitation retrievals.

The product is offered in three stages: Early Run, Late Run, and Final Run. Researchers are encouraged to utilize the Final Run data for comprehensive analyses, as this stage incorporates monthly gauge data to create research-level products. However, it is important to note that the Final Run data has a latency period of approximately 3.5 months from the time of observation. Accordingly, we will employ the Final Run product, specifically

---

<sup>3</sup><[https://arthurhou.pps.eosdis.nasa.gov/Documents/IMERG\\_TechnicalDocumentation\\_final.pdf](https://arthurhou.pps.eosdis.nasa.gov/Documents/IMERG_TechnicalDocumentation_final.pdf)>

using the NASA Goddard Earth Sciences (GES) Data and Information Services Center (DISC) V07 data, accessible through the link <sup>4</sup>, last accessed on 16 May 2025, which offers precipitation data in netCDF format.

Lastly, concerning temporal distribution, this dataset, which covers the period from June 2000 to September 2021, is available for download every half-hour, daily, or monthly. For our analysis, we intend to concatenate the data to create hourly aggregates from the half-hourly product, which will subsequently be extrapolated to a resolution of approximately 30 km (our forecast resolution).

### 3.1.4 GPM-MERGIR

In the context of convective cloud modeling, it is essential to evaluate the model's capability to accurately represent cloud morphology. This assessment can be achieved through the analysis of infrared (IR) brightness temperature (Tb), also known as equivalent black-body temperature, using satellite data. The observational dataset we are currently employing comes from the NASA GES DISC GPM Merged 4-Km IR Tb data set (GPM-MERGIR) (JANOWIAK et al., 2017), which is sourced from the NOAA Climate Prediction Center (CPC)/NCEP/NWS. The satellites contributing to this dataset include the Geosynchronous Operational Environmental Satellites (GOES) from the United States, the Geosynchronous Meteorological Satellite (GMS), followed by the Multi-functional Transport Satellite (MTSat) and Himawari from Japan, as well as the Meteorological Satellite (Meteosat) from the European Community, which forwards infrared (IR) imagery to the CPC. A complete list of these satellites can be found at this link <sup>5</sup>.

The data is made available periodically in half-hour increments, covering latitudes from 60°S to 60°N with a pixel resolution of 4 km, dating back to 1 January 1998. In addition to direct downloads of netCDF-4 format data, GES DISC also provides data in binary, ASCII, and netCDF-3 formats via the OPeNDAP interface.

### 3.1.5 GSMAp

Another satellite-based combined microwave-IR precipitation dataset will be utilized to evaluate precipitation generated by tropical cyclones. The Global Satellite Mapping of Precipitation (GSMAp), supported by the JAXA Precipitation Measuring Mission (PMM) Science Team, offers a multi-satellite global precipitation map as part of the Global Precipitation Measurement (GPM) Mission. It employs the Dual-frequency Precipitation Radar (DPR) onboard GPM core satellites, along with other GPM constellation satellites and geostationary satellites (website). Additionally, in the GSMAp products, apart from

---

<sup>4</sup><<https://gpm.nasa.gov/data/directory>>

<sup>5</sup><<https://docserver.gesdisc.eosdis.nasa.gov/public/project/GPM/CPC-4kmIR-Sats.pdf>>

GSMaP\_NOW, the Globally-merged, full-resolution ( $\sim$  4km) infrared data produced by NOAA/CPC has also been utilized<sup>6</sup>. The original data used for this product have been supplied by JAXA's GSMAp.

The key feature of the GSMAp algorithm is its use of various attributes derived from the spaceborne precipitation radar, including TRMM/PR and GPM/DPR. This algorithm generates a rainfall rate product (in mm/hr) that covers a global extent (60°N to 60°S) with a horizontal resolution of 0.1° (latitude/longitude) and is available on an hourly basis.

The differences, features, and performance of this dataset compared to GPM-IMERG in tropical cyclone cases are widely discussed in the literature (REDDY et al., 2022; BAGTASA, 2022; YANG et al., 2024).

### 3.2 Numerical model: MONAN

The model utilized for this study is part of the next generation of numerical models currently under development. The Model for Ocean-LaNd-Atmosphere Prediction (MONAN) is an advanced project by the Brazilian Centre of Weather and Climate Prediction (CPTEC) to become the new standard for weather and climate forecasting, nowcasting, and hindcasting. MONAN is an adaptation of the Model for Prediction Across Scales (MPAS), and further details will be provided in the subsequent paragraphs.

The MONAN is a collaborative initiative led by the National Institute for Space Research (INPE) and the Ministry of Science, Technology, and Innovation (MCTI). Its primary objective is to improve weather and climate forecasting in Brazil, South America, and the Caribbean at all spatial and temporal scales, particularly in climate change scenarios.

MONAN employs an MPAS (Model for Prediction Across Scales) dynamical core, supplemented by various physics innovations developed by the scientific community. The most recent version of MONAN is 1.0.0 (last seen on July 2, 2024) with ongoing enhancements available for review at <https://monanadmin.github.io/>.

Regarding the physics suite, MPAS offers two configurations: "Mesoscale Reference" and "Convection-permitting," which vary based on resolution. The Mesoscale Reference is suitable for mesoscale resolutions (greater than 10 km cell spacing; i.e.,  $dx > 10$  km) but, as noted in the MPAS manual<sup>7</sup>, is not ideal for convective-scale simulations since the Tiedtke scheme can eliminate convective instability before the resolved-scale motions (convective cells) can effectively respond. On the other hand, the Convection-permitting option is designed for spatial resolutions that accommodate both explicitly resolved hydrostatic and

---

<sup>6</sup>These details were obtained from the documentation available at <<https://sharaku.eorc.jaxa.jp/GSMaP/guide.html#01>>.

<sup>7</sup>[https://www2.mmm.ucar.edu/projects/mpas/mpas\\_atmosphere\\_users\\_guide\\_7.0.pdf](https://www2.mmm.ucar.edu/projects/mpas/mpas_atmosphere_users_guide_7.0.pdf)

nonhydrostatic motions. This suite is recommended for any MPAS applications employing convection-permitting meshes ( $dx < 10$  km), including variable-resolution meshes that span hydrostatic to nonhydrostatic resolutions.

For our simulations ( $15\text{km} < dx < 60\text{km}$ ), the current physics parameters are summarized in the table below:

Table 3.3 - Physics bulk configuration

Parameter	Configuration
Mesoscale reference (30 km)	
Microphysics	WSM-6
Convection	Grell-Freitas MONAN
Boundary layer (BL)	MYNN
Gravity wave drag by orography	YSU
Longwave radiation (LW)	RRTMG
Shortwave radiation (SW)	RRTMG
Cloud fraction for radiation	Cloud Fraction Monan
Surface layer	MYNN
Land surface	Noah

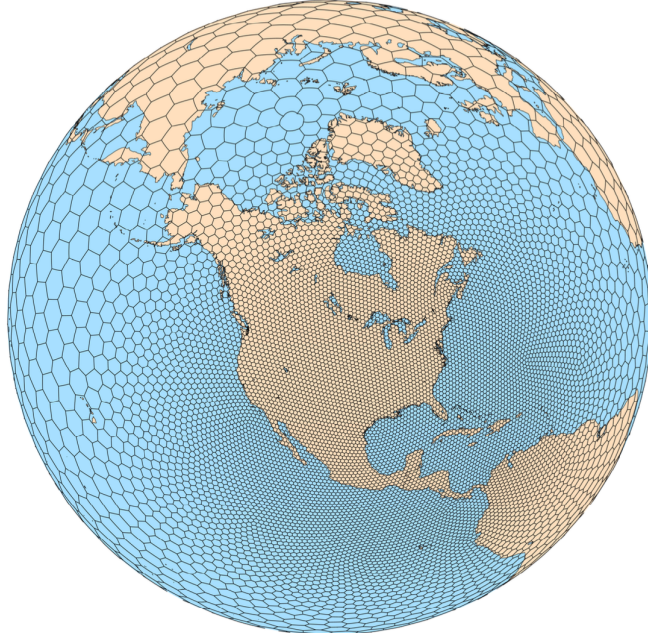
Source: Made by the author (2025).

The cloud microphysics utilizes the single-moment 6-class scheme as described by [Hong e Lim \(2006\)](#). The convection parameterization, based on the mass-flux approach developed by [Grell e Freitas \(2014\)](#) and [Freitas et al. \(2018\)](#), is implemented here along with the cold pool scheme proposed by [Freitas et al. \(2024\)](#). Both the Planetary Boundary Layer (PBL) and Surface Layer parameterizations employ the [Nakanishi e Niino \(2009\)](#) level 2.5 closure turbulent kinetic energy (TKE) based scheme. Orographic gravity-wave drag is represented using the Yonsei University (YSU) PBL scheme. For solar (shortwave) and terrestrial (longwave) radiative transfers, the Rapid Radiative Transfer Model for GCMs ([IACONO et al., 2008](#)) radiation scheme is utilized. Finally, the Land Surface parameterization is based on the [Mitchell \(2005\)](#) model.

All simulations were conducted globally, utilizing a uniform horizontal grid spacing dependent on the specific experiment, which was set at 15 km, 30 km, and 60 km. The model has 55 vertical levels, with the ocean reference set at depths of 0 m and 30000 m (30 km). Due to the global scope, only a single initial condition was required, sourced from the ERA5 and GFS models. The duration of the model time integration varies according to the experiment and will be detailed in the results section, along with the initial time of integration. Figure 3.1 displays a map generated with MPAS-A and Figure 3.2 a map of

convective rain accumulated of 2 days forecasted by MONAN.

Figure 3.1 - MPAS-A meshes and the ability to configure the meshes at different resolutions.



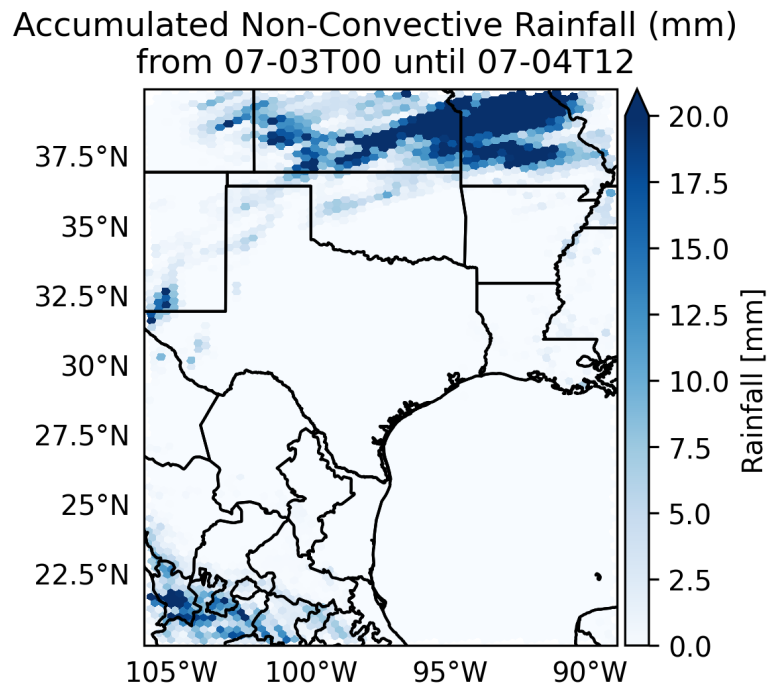
Source: <<https://www2.mmm.ucar.edu/projects/mpas/site/visualization.html>> (2025) .

As one can see, one of the big differences between MPAS and its predecessor, the WRF model, is that the model is discretized on centroidal Voronoi meshes using a C-grid staggering of the prognostic variables, allowing variable horizontal resolution, and also solving the equations of motion directly on these unstructured meshes ([SKAMAROCK et al., 2012](#)).

For our study, a set of variables was chosen to perform it. Table 3.4 indicates the variable name inside MONAN, alongside with the long name and the unit.

Total rainfall was computed by simply summing the variables rainnc and rainc for each lat/lon point. The wspd is the module of the squared sum of zonal and meridional winds at the first model level. From uzonal\_200hPa below, all variables are computed at the reference level pressure; for instance, uzona\_200hPa means the zonal wind at the pressure level of 200hPa.

Figure 3.2 - 30km horizontal resolution at native mesh in MONAN.



Source: Made by the author (2025) .

Table 3.4 - MONAN Atmospheric Variables Selected for Model Evaluation

Variable name	Long name	Unit
rainc	Convective rainfall	mm/h
rainnc	Not Convective rainfall	mm/h
mslp	Mean sea level pressure	hPa
wspd	Wind speed	m/s
ctt	Cloud top temperature	°C

Source: Made by the author, 2025.

### 3.2.1 Initial condition generation

To begin the integration process, Initial Conditions (IC) must be prepared by MPAS requirements, which can be found at the footnote of this page <sup>8</sup> <sup>9</sup>. We generated the initial conditions using the Weather Research & Forecasting Model (WRF) Pre-Processing System (WPS), utilizing data obtained from ERA5, which we pre-processed with the WPS. These initial conditions were then uploaded into the MONAN IC folder and executed accordingly. For the IC sensitivity test, we also acquired a GRIB file from the Global Forecast System (GFS) model, a courtesy provided by Saulo R. Freitas, who already had the data available. The model will initially be set up with a global 30 km MPAS grid, with plans to modify this in future sections. It is important to note that a new IC will need to be created for each resolution.

### 3.2.2 Post-processing

Since the model output is generated on a non-structured grid, a post-processing step is necessary to map the native MPAS output to other meshes, enabling visualization on a standard lat/lon map. To achieve this, MONAN employs the convert-MPAS project <sup>10</sup>. This approach utilizes a nearest-neighbor scheme to remap integer fields to the target grid, with additional information available at this link.

In this study, the Climate Data Operators (CDO) were also utilized to remap various datasets, including ERA5, GPM-IMERG, GPM-MERGIR, and GSMap, as well as several forecasts (such as those simulated at 15km and 60km horizontal resolutions) to the MONAN forecasts.

---

<sup>8</sup><[https://www2.mmm.ucar.edu/projects/mpas/site/documentation/users\\_guide/running.html](https://www2.mmm.ucar.edu/projects/mpas/site/documentation/users_guide/running.html)>

<sup>9</sup><[https://www2.mmm.ucar.edu/projects/mpas/mpas\\_atmosphere\\_users\\_guide\\_7.0.pdf](https://www2.mmm.ucar.edu/projects/mpas/mpas_atmosphere_users_guide_7.0.pdf)>

<sup>10</sup><[https://github.com/mgduda/convert\\_mpas](https://github.com/mgduda/convert_mpas)>



## 4 METHODOLOGY: METRICS AND DIAGNOSTIC FIELDS

Our methodology is designed based on three main characteristics of tropical cyclones commonly utilized in weather forecasting: track, intensity, and rainfall. The metrics that are currently used in similar studies will be described accordingly to each category. Then, for each hurricane, a table with addressed questions will be shown to guide the reader in the analysis and discussion of the results. This table will be part of the workflow, a diagram that shows the steps and figures/maps that will be created. All code made for this dissertation is available on the [GitHub - Dissertation Repository](#), mainly written in Python.

### 4.1 Trajectory

A map illustrating the forecasted trajectories will be generated using a tracking algorithm developed by the author. A discussion regarding the performance of this tracking and guidance can be found in Appendix A. Additionally, a time series analysis will be conducted to evaluate the errors associated with each trajectory. These errors are defined as the distance between the central pressure reference points and the forecasted central pressure points, calculated using the GeoPy library<sup>1</sup>. As noted in the literature, the calculations could be performed following the methodology proposed by Moon et al. (2021) but here we simply calculate the great-circle distance between two points.

To quantitatively validate the results, a graphical representation will display the Mean Absolute Error (MAE) and Root Mean Square Error (RMSE) for each of the trajectories, regarding the reference dataset.

The MAE is widely employed ([DITCHEK et al., 2023; NYONGESA et al., 2024](#)) in the literature and can be defined as:

$$\text{MAE} = \frac{1}{N} \sum_{i=1}^N |F_i - O_i| \quad (4.1)$$

in this equation,  $N$  represents the sample size (number of points in the trajectory),  $F$  denotes the forecast outputs generated by the model, and  $O$  refers to the observation outputs obtained from a reference dataset. The error values can range from 0 to  $\infty$ , with a perfect score indicated by 0. The aim is to calculate the average magnitude of the forecast errors. It is important to note that this error does not convey the direction of the deviations due to its absolute nature; this aspect will be examined using another method discussed later.

---

<sup>1</sup><https://geopy.readthedocs.io/en/stable/>

Along with the MAE, usually, RMSE is computed to seek a kind of average error, but now weighted according to the square of the error. As the same as before, it varies from 0 to  $\infty$ , and a perfect score means RMSE equal to 0. It is defined as:

$$\text{RMSE} = \sqrt{\frac{1}{N} \sum_{i=1}^N (F_i - O_i)^2} \quad (4.2)$$

The letters in this equation have the same meaning as in the previous equation. To better understand the potential trends in the trajectory, in addition to visual comparisons, one can utilize cross-track and along-track errors computed into a time series. The errors assess the deviation of the forecasted position from the observed path (cross-track) and the speed of the forecast from the observations (along-track). The cross-track error is measured perpendicularly to the observed trajectory, while the along-track error is measured along the actual course at a specified event. Together, these metrics<sup>2</sup> can also indicate the directional error of each forecast. Figure 4.1 more clearly illustrates the distinction between cross-track and along-track errors.

In the context of our expected findings, negative (positive) values of cross-track errors indicate that the forecasted center of the hurricane is projected to be located to the west (east), while negative (positive) values of along-track errors suggest that the center is slower (faster) than its intended trajectory.

Such errors can be further investigated through the analysis of meteorological fields, as demonstrated by Gao et al. (2023). For example, examining the 700 hPa geopotential height can help identify large-scale features that contribute to tracking biases. In their study, forecasts exhibiting a pronounced eastward track bias for tropical cyclones were often associated with a notably weaker subtropical high over the North Atlantic. Although this work does not include such an approach due to time constraints, it represents a different approach for future research and is highlighted here for reference.

In conclusion, utilizing a straightforward statistical mean of the errors (specifically the MAE and RMSE) can provide valuable insights into the overall performance of the MONAN simulations. The mean is defined as follows:

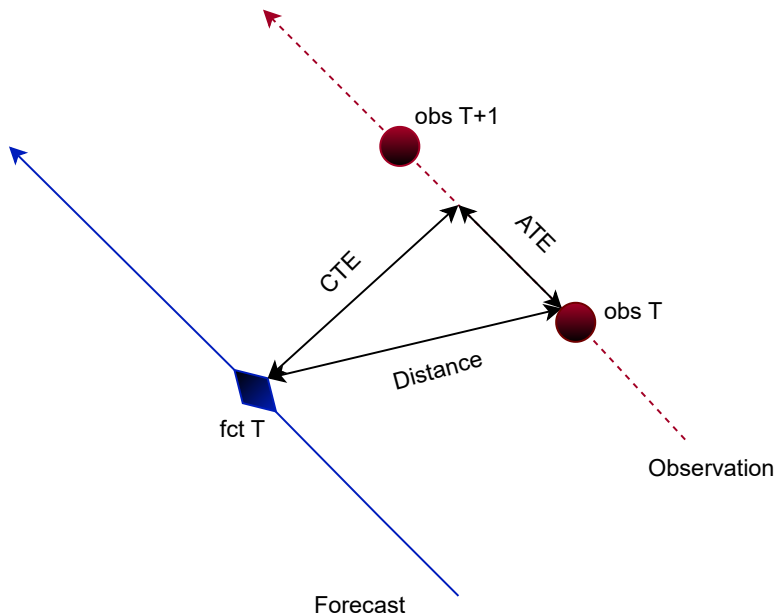
$$\text{MEAN} = \frac{1}{E} \sum_{i=1}^E \text{errors}_i \quad (4.3)$$

where E denotes the total number of experiments conducted using the MONAN framework.

---

<sup>2</sup>The equations used to compute those errors can be found at this website: <<https://www.movable-type.co.uk/scripts/latlong.html>>

Figure 4.1 - Illustration of cross-track and along-track errors. The definitions of Cross-Track Error (CTE) and Along-Track Error (ATE) are based on the distance between an observation (obs) and a forecast (fct) at the same valid time (T). This distance is computed as the great-circle distance.



Source: Made by the author (2025).

This approach facilitates a comprehensive understanding of the general behavior exhibited by the MONAN runs and can be compared with ERA5, for instance.

## 4.2 Intensity

In reviewing the literature, tropical cyclone intensity is defined as the maximum surface wind speed associated with the central pressure (DEMARIA et al., 2007; LANDSEA; FRANKLIN, 2013). However, some studies argue that depending exclusively on wind speed does not fully capture the concept of intensity, suggesting that pressure can also serve as a significant indicator of forecasted intensity (SHEPHERD; WALSH, 2017; HEMING, 2017). This dissertation will adopt the latter approach by evaluating both pressure and wind as intensity indicators.

To conduct these evaluations, we will analyze time series data that includes the central pressure identified by the tracking system and the maximum wind speed, which is derived from the first level of the model. A discussion on how to determine this maximum wind speed in the model can be found in Appendix A. The time series will serve as a measure

of forecast performance, allowing us to assess how closely the computed values align with actual observations and where they occur.

In addition to a visual comparison, we will create a graph containing the MAE and RMSE to quantify the forecasts and rank them based on their effectiveness in illustrating intensity. Additionally, the mean of those errors can also be computed and compared with ERA5 to give us insights into the general MONAN performance.

### 4.3 Rainfall

The analysis of rainfall for our runs is based on the methodology proposed by [Marchok et al. \(2007\)](#). According to these authors, evaluating forecasted rainfall requires examining three key aspects: the rainfall pattern, the mean and distribution of rain volume, and the extreme values.

To investigate the rainfall pattern, we will utilize the Equitable Threat Score (ETS; [Mesinger \(2008\)](#)) along with pattern correlation analysis (namely the Pearson Correlation Coefficient) and visual comparisons using selected snapshots, considering also the related bias of those fields. The mean and distribution of rain volume can be assessed through the computation of the Cumulative Density Function (CDF) and the Probability Density Function (PDF). Extreme rainfall values will be specifically analyzed by examining the 85th percentile computed at the CDF. Lastly, we will discuss a performance score for MONAN in comparison to ERA5 by averaging the results of all experiments. Table 4.1 summarizes the metrics to be computed, followed by a brief explanation of each metric and its intended purpose.

Table 4.1 - Metrics used to evaluate rainfall forecast performance

Metric	Definition
ETS (Equitable Threat Score)	Measures the skill of categorical forecasts by comparing the number of hits to what would be expected by chance: $ETS = \frac{H - H_r}{H + F + M - H_r}$ where $H$ is the number of hits, $F$ is false alarms, $M$ is misses, and $H_r = \frac{(H+F)(H+M)}{total}$ is the expected number of hits due to chance.
Pearson Correlation Coefficient	Measures the spatial similarity between observed and forecasted rainfall fields: $r = \frac{\sum_{i=1}^n (F_i - \bar{F})(O_i - \bar{O})}{\sqrt{\sum_{i=1}^n (F_i - \bar{F})^2 \sum_{i=1}^n (O_i - \bar{O})^2}}$ where $F$ and $O$ are forecasted and observed values, calculated over $n$ data points, where $i$ is the index running from 1 to $n$ .
Bias	Quantifies the difference between forecast and observation: $\text{Bias} = F - O$
CDF (Cumulative Distribution Function)	Represents the probability that a variable takes a value less than or equal to a given threshold: $\text{CDF}(x) = P(X \leq x)$
PDF (Probability Density Function)	Describes the relative likelihood for a variable to take a specific value: $\text{PDF}(x) = \frac{d}{dx} \text{CDF}(x)$

Source: Made by the author (2025).

The ETS evaluates how well forecasted “yes” events correspond to observed “yes” events, while accounting for agreements due to random chance. According to [Marchok et al. \(2007\)](#), this implies that the ETS penalizes a model for overproducing rainfall above a given threshold, even if the rainfall pattern is realistic. For this metric, a hit is defined as an event that was forecasted to occur and did occur; a miss is an event that was not forecasted but occurred; and a false alarm is an event that was forecasted but did not occur.

Pattern correlation is computed as the Pearson correlation coefficient ( $r$ ) between the forecasted and observed rainfall fields. The correlation ranges from -1 to 1, where: (i)  $r = 1$  indicates a perfect positive linear relationship; (ii)  $r = -1$ , a perfect negative linear relationship; and (iii)  $r = 0$  implies no linear relationship between forecast and observation.

The bias is the difference between the forecast ( $F$ ) and the observations ( $O$ ), typically averaged over time or space. A negative bias indicates underestimation, while a positive bias indicates overestimation. The bias can range from negative to positive infinity, with 0 representing a perfect forecast.

Both the CDF and the PDF will be used to analyze rainfall distributions. The CDF shows the cumulative probability of rainfall values up to a certain threshold. For example, the corresponding x-axis value when the y-axis equals to 0.5 (or 50%) on the CDF corresponds to the median rainfall amount. The CDF ranges from 0 to 1 on the y-axis, indicating the proportion of the data below a given threshold on the x-axis. For instance, the 0.85 mark on the CDF corresponds to the 85th percentile, meaning 85% of the data falls below that threshold, and the remaining 15% above it. This is a straightforward way to seek for rainfall extremes.

The PDF, similar to a histogram, describes the probability of observing values within a specific range. It is normalized such that the total area under the curve equals 1. To interpret the PDF, one can compute the area under the curve within a specified range, which represents the probability of a value falling in that interval. Mathematically, the CDF is the integral of the PDF. One should notice that both CDF and PDF can be computed empirically or theoretically. The difference between them is that when computing empirically, one will consider the natural distribution of data, and theoretically, one will consider a mathematical distribution (gamma, Gaussian, etc). In this study, we will utilize the empirical approach.

#### 4.4 Hurricane Beryl workflow

With the hurricane Beryl event, the goal is to investigate the cold pool parameterization alongside sensitivity tests, and with those sensitivity tests, select an optimal parameter configuration for the parameterization.

The table below outlines the questions designed to guide the examination of each characteristic in alignment with the dissertation's objectives. This approach will help refine the discussion and outputs available in the existing literature.

Table 4.2 - Key Research Questions for Track, Intensity, and Rainfall Assessment

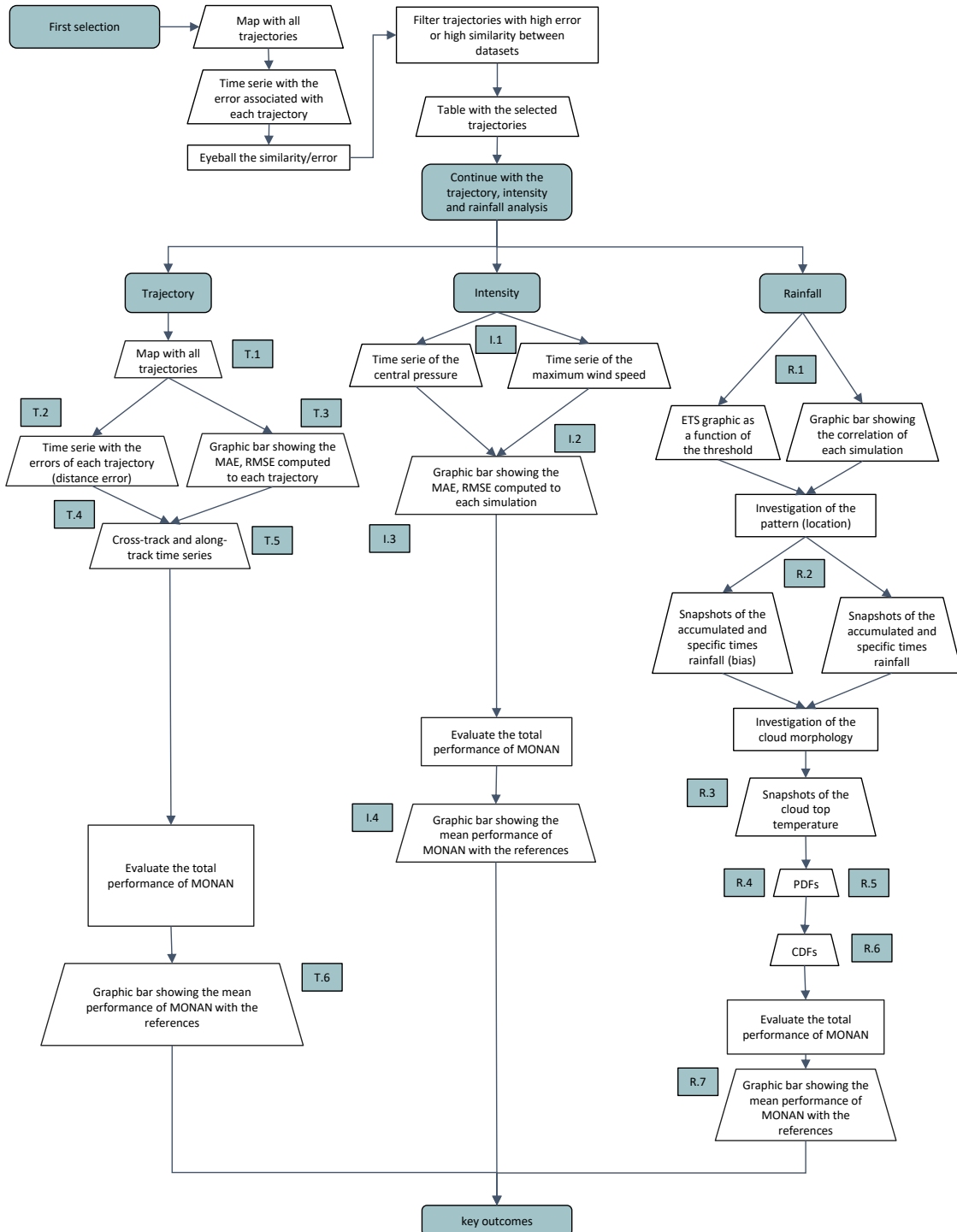
Topic	Question	ID
Trajectory	What is the overall performance of the parameterization and sensitivity tests in reproducing the hurricane's track?	T.1
	What is the error (in kilometers) associated with these tracks?	T.2
	Which configuration shows the best performance?	T.3
	After how many forecast hours do larger deviations begin to appear?	T.4
	Is there any observable trend in the tracks?	T.5
	What is the overall performance of MONAN?	T.6
Intensity	What is the overall performance of the parameterization and sensitivity tests in reproducing the hurricane's intensity?	I.1
	How much bias is present in these results?	I.2
	How well does ERA5 perform in reproducing this intensity, and why?	I.3
	What is the overall performance of MONAN?	I.4
Rainfall	What is the overall performance of the parameterization and sensitivity tests in reproducing the hurricane's rainfall pattern?	R.1
	In which regions is there a negative (or positive) bias in the rainfall field?	R.2
	What is the overall performance of the parameterization and sensitivity tests in reproducing the hurricane's cloud morphology?	R.3
	How much light, moderate, and heavy rainfall is being produced by the simulations?	R.4
	What is the average rainfall produced by the simulations?	R.5
	What is the bias between the extreme rainfall produced by the simulations and the reference data?	R.6
	What is the overall performance of MONAN?	R.7

Source: Made by the author (2025).

The workflow below summarizes and organizes the upcoming steps. After a quick initial analysis, the results will be visually represented as trapezoidal shapes, while discussions will be depicted with rectangular shapes. This distinction helps clarify the types of information being presented at each stage of the process. Following this, the boxes containing question IDs, as outlined in Table 4.2, related to the three aspects under evaluation (trajectory, intensity, and rainfall) will be also displayed in the workflow.

The reader should note that an initial selection of the results will be conducted. As the

Figure 4.2 - Workflow Overview of Hurricane Berry



Source: Made by the author (2025).

diagram indicates, a trajectory map will be created, accompanied by distance errors. The selection criteria will focus on experiments that do not contribute significantly to the discussion, either because they are part of a set of similar experiments or due to excessively large errors that do not accurately represent the model state we aim to address.

#### 4.5 Hurricane Helene workflow

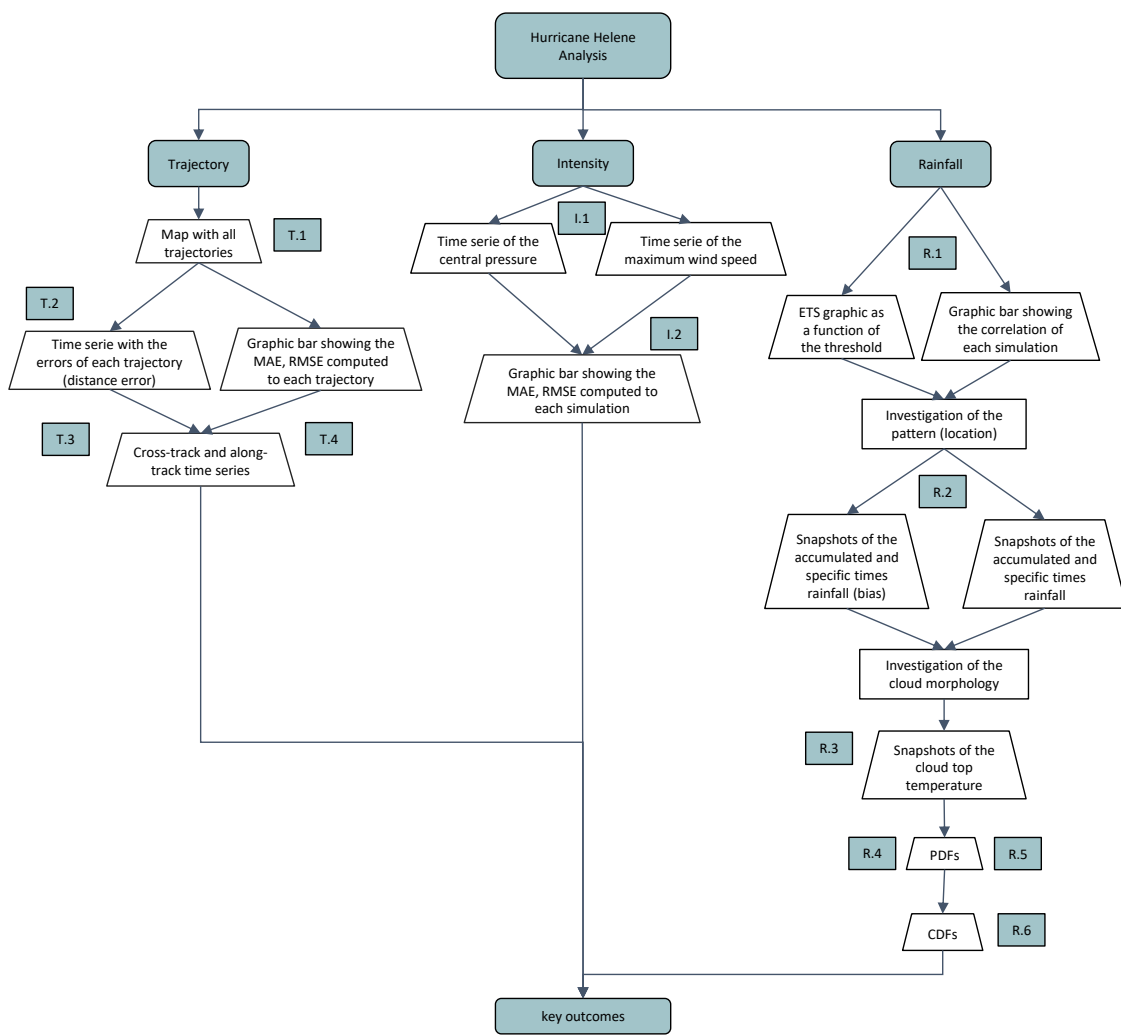
Now we aim to test the best configuration alongside the cold pool effect and the highest resolution effect in another hurricane, Helene. Table 4.3 indicates the questions addressed for this investigation and furthermore, a similiar diagram as designed in the previous section were made here.

Table 4.3 - Key Research Questions for Track, Intensity, and Rainfall Assessment

Topic	Question	ID
Trajectory	What is the overall performance of the optimal configuration found, the parameterization, and the high-resolution effect in reproducing the hurricane's track?	T.1
	What is the error (in kilometers) associated with these tracks?	T.2
	After how many forecast hours do larger deviations begin to appear?	T.3
	Is there any observable trend in the tracks?	T.4
Intensity	What is the overall performance of the optimal configuration found, the parameterization, and the high-resolution effect in reproducing the hurricane's intensity?	I.1
	How much bias is present in these results?	I.2
Rainfall	What is the overall performance of the optimal configuration found, the parameterization, and the high-resolution effect in reproducing the hurricane's rainfall pattern?	R.1
	In which regions is there a negative (or positive) bias in the rainfall field?	R.2
	What is the overall performance of the optimal configuration found, the parameterization, and the high-resolution effect in reproducing the hurricane's cloud morphology?	R.3
	How much light, moderate, and heavy rainfall is being produced by the simulations?	R.4
	What is the average rainfall produced by the simulations?	R.5
	What is the bias between the extreme rainfall produced by the simulations and the reference data? Do the forecasts capture the extreme event in North Carolina?	R.6

Source: Made by the author (2025).

Figure 4.3 - Workflow Overview of Hurricane Helene



Source: Made by the author (2025).

## 5 CASE STUDY: HURRICANE BERYL

This chapter explores the results of implementing cold pool parameterization in the latest Brazilian numerical weather and climate prediction model, MONAN. It emphasizes the model's performance in predicting hurricane trajectory, intensity, and rainfall, using Hurricane Beryl as a case study, which occurred between June and July 2024 in the North Atlantic Basin. Following a brief introduction to the event, the chapter presents the results of the forecast and offers a direct comparison between ERA5 and MONAN. Finally, a discussion section will address the questions outlined previously in Table 4.2.

### 5.1 Event description - hurricane Beryl

Hurricane Beryl formed in the deep tropical Atlantic's Main Development Region on June 28th, forming a tropical depression near 1200 UTC 28 June about 1200 nautical miles <sup>1</sup> east of Barbados, with a center at 1007 mb and wind speed of 30 kts. According to reports from the National Oceanic and Atmospheric Administration (NOAA), the storm rapidly intensified into a major hurricane, moving eastward and ultimately reaching Category 5 on the Saffir-Simpson Hurricane Wind Scale, making it the earliest Category 5 hurricane on record in the Atlantic Basin. Figure 5.1 display all the trajectory computed with the best track dataset.

It is important to note that the figure presented in the upper-right quadrant indicates critical meteorological parameters, including the peak wind speed recorded at 145 knots, the minimum mean sea level pressure of 934 hPa, and the Accumulated Cyclone Energy (ACE), which is quantified at 34.5. These values are derived directly from the best track dataset.

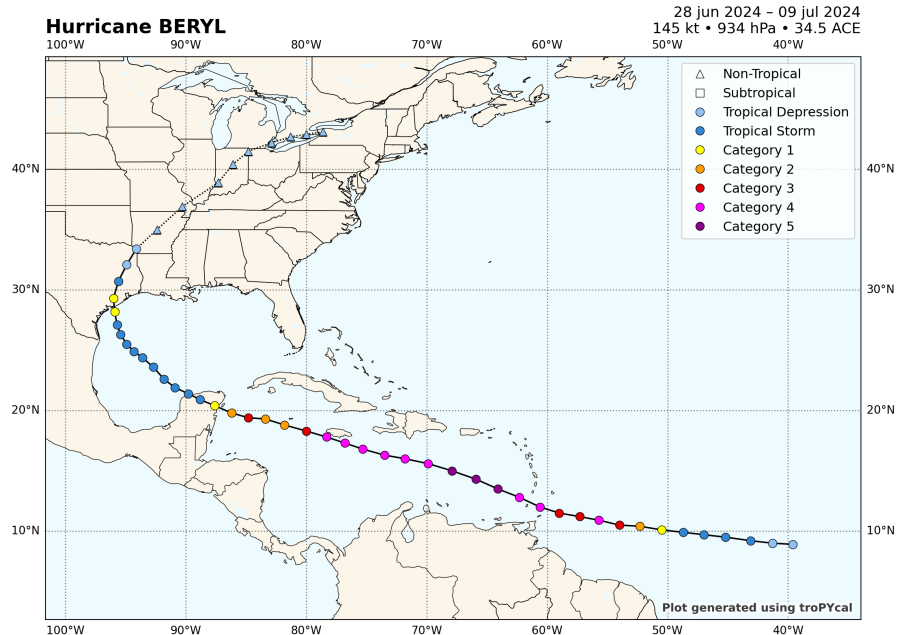
The first landfall of Hurricane Beryl occurred on the island of Carriacou in Grenada as a high-end Category 4 storm on July 1st, subsequently intensifying to a Category 5 in the Eastern Caribbean Sea. From a disaster perspective, the total damages in the Grenada Region are significant, with estimates of approximately US\$ 218.0 million, which accounts for about 16.5 percent of the GDP for 2023 ([GUNASEKERA et al., 2024](#)). Satellite images illustrating the hurricane's transition from Category 4 to Category 5, passing through the first landfall, are presented in Figure 5.2.

At the passage through the Caribbean region, the rainfall was more intense in Jamaica, with widespread totals between 8 to 12 inches, and a peak of 13.62 inches observed at Knockpatrick in Manchester Parish, representing the highest storm-total rainfall reported.

---

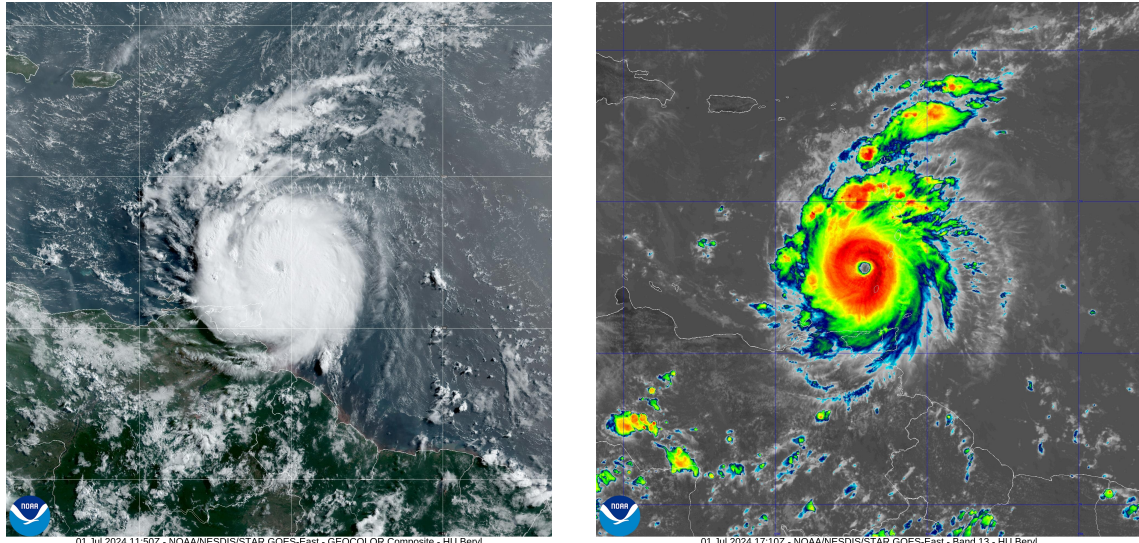
<sup>1</sup>In North American meteorology, it is common to use: pressure in millibars (mb), where 1 mb = 1 hPa; distance in nautical miles (nm), where 1 nm = 1.852 km; wind speed in knots (kt), where 1 kt = 1.852 km/h; and precipitation in inches (in), where 1 inch = 25.4 mm

Figure 5.1 - 2024 Hurricane path according to best track analysis



Source: Made by the author (2025).

Figure 5.2 - Hurricane Beryl view from the GEOCOLOR composite (left) and Band 13 (right) when passing through the first landfall

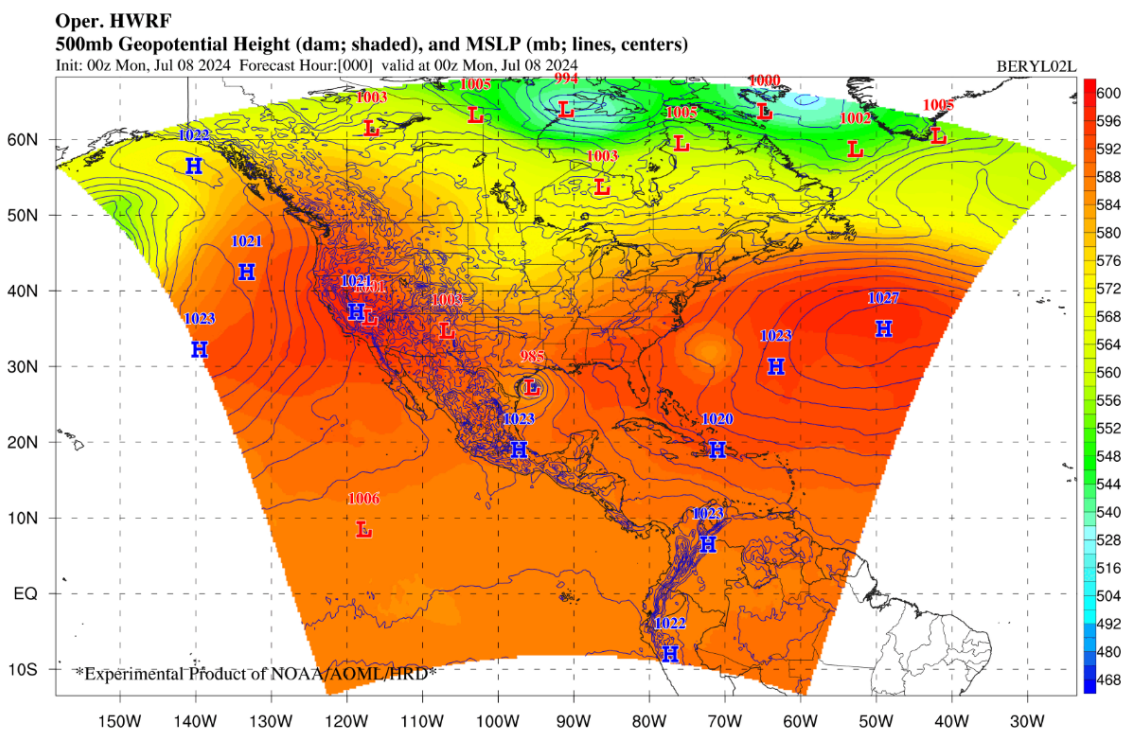


Source: <<https://www.star.nesdis.noaa.gov/star/index.php>>

The storm began to weaken before making a second landfall on the Yucatán Peninsula

as a high-end Category 2 hurricane early on July 5th. Following its passage through the Peninsula, the hurricane continued to weaken while moving northwest, influenced by a large mid to upper-level trough of low pressure over the Central U.S., which eroded the robust ridge of high pressure over the Gulf of Mexico (LI et al., 2025). The combination of increasing wind shear and dry air entrainment maintained a nearly steady state until dawn on July 7th. Later that morning, Hurricane Beryl progressed toward the Central Texas coast (northwest) as the mid to upper-level trough deepened to the north. An influx of moisture and decreased wind shear allowed the storm to become better organized, resulting in it being classified as a Category 1 hurricane by 11 PM CDT on July 7th (04:00 UTC on July 8th). A glimpse of this large scale environment is shown at Figure 5.3.

Figure 5.3 - 500 mb Geopotential Height and MSLP at July 8th, 00:00 UTC

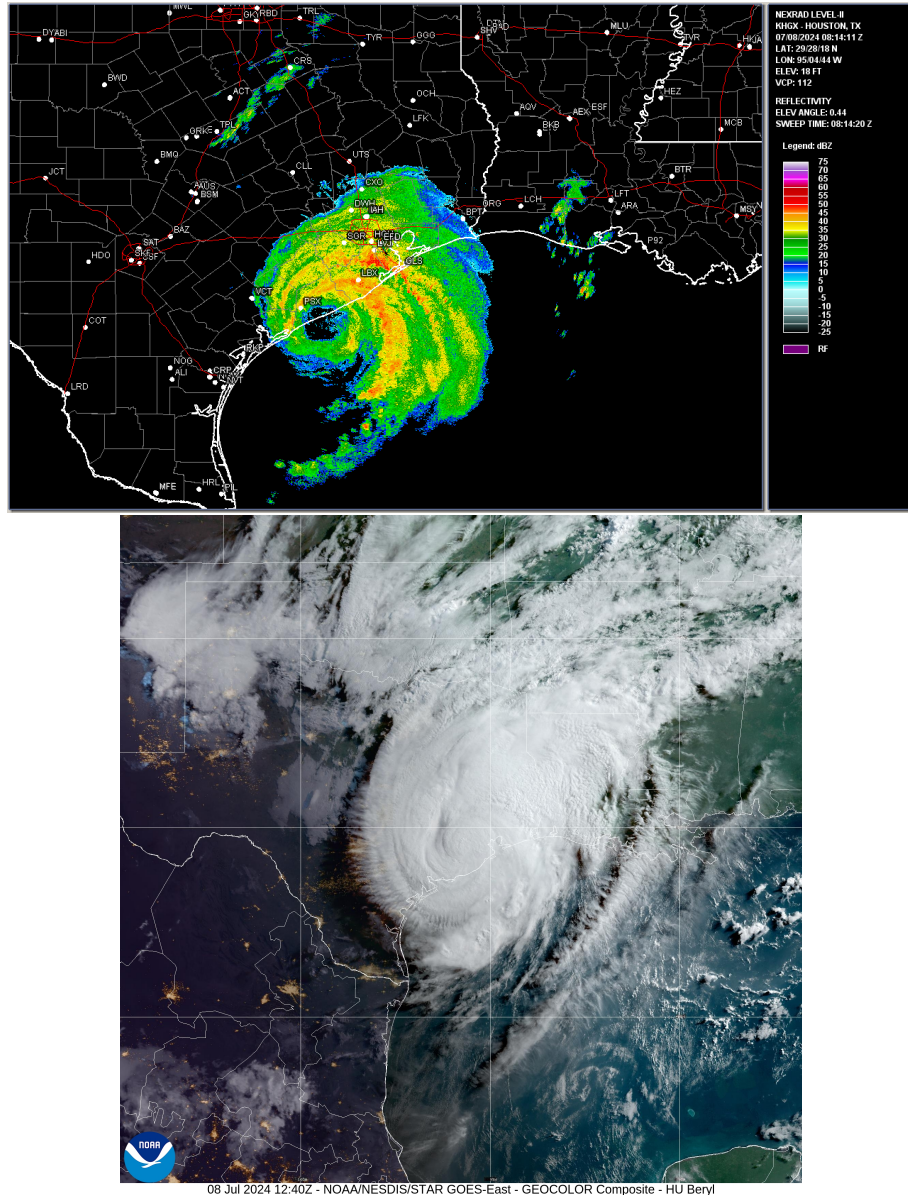


Source: <<https://storm.aoml.noaa.gov/viewer/?projectName=BASIN>>.

At approximately 4 AM CDT on July 8th (09:00 UTC on July 8th), the hurricane made landfall near Matagorda along the Texas coast. Its maximum sustained winds were about 129 km/h (80 mph), and its minimum central pressure was 979 hPa. Figure 3 shows satellite and radar imagery capturing Hurricane Beryl's approach to the Texas coast.

Finally, the storm began to shift north-northeast, becoming a tropical storm by 10 AM CDT (15:00 UTC on July 8th). As it moved through the continental region, it weakened and transitioned to a tropical depression by 10 PM CDT (03:00 UTC on July 9th), just

Figure 5.4 - HB view from NEXRAD (top) and GEOCOLOR composite (bottom) when reaching the Texas Coast.



Source: <<https://www.star.nesdis.noaa.gov/star/index.php>>.

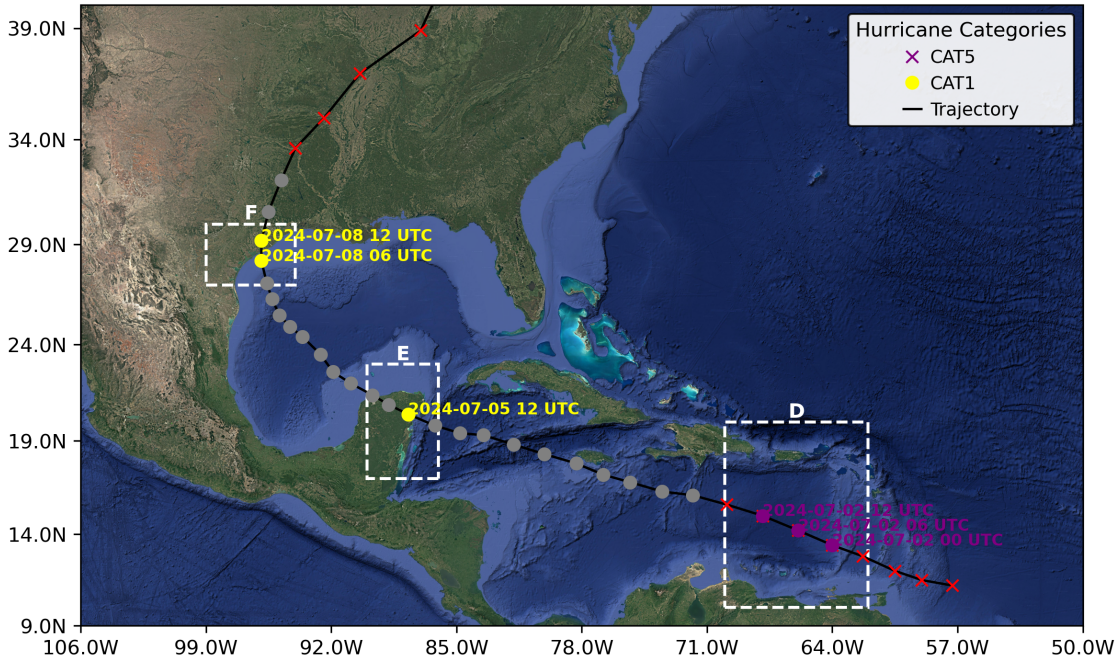
northwest of Shreveport, Louisiana.

Over the United States, the most intense rainfall occurred in the Houston metropolitan area in southeastern Texas, where widespread totals ranged from 8 to 12 inches, with local maxima of 14.99 inches in Thompsons and 14.88 inches at a HCFCD station in western Houston (LI et al., 2025).

Based on this overview of the storm, Figure 4 has been created to illustrate the study area

of interest, highlighting the significant landfalls made during its progression.

Figure 5.5 - Spatial Domain of Hurricane Beryl's Development and Trajectory.



Source: Made by the author (2025).

The observational period for this study encompasses a six-day interval from 00 UTC on July 3 to 00 UTC on July 9, 2024, as illustrated by the gray bullet points in Figure 5.5. Notably, this analysis will focus on a post-Category 5 storm. Whereas the system was active from June 28 to July 9, our analysis concentrates primarily on this specific timeframe. A sensitivity analysis regarding an earlier forecast of the observation period will be conducted and discussed in subsequent sections. This study encompasses significant geographical features, including the passage through Jamaica, which recorded the highest levels of rainfall in the Caribbean, the Yucatan landfall as denoted by the square E in Figure 5.5, and the subsequent landfall in Texas, indicated by the square F in Figure 5.5.

## 5.2 Results and analysis of hurricane Beryl

In this section, we will present the results in alignment with the established workflow and engage in a discussion regarding the questions outlined in Table 4.2. The subsequent subsections will detail the trajectory, intensity, and rainfall analyses. To conclude, we will provide a summary discussion highlighting the key outcomes of the model and evaluating the overall performance of MONAN in comparison with ERA5 reanalysis.

By the workflow sequence, we will begin by addressing the selection process. Table 5.1

illustrates all the experiments that were conducted.

Table 5.1 - All performed experiments

Experiment	Description	ID
Cold Pool Effect	Turn on and off the cold pool parameterization scheme	CP-ON CP-OFF (Control)
Initial Condition Day	Compares the effect of two initial conditions, June 29, July 2nd (noon), and July 3rd. Tested with 1st July	CP-29 CP-01 CP-02T12 CP-03
Cold Pool Lifetime	Compares the effect of cold pool life time being 1h, 2h (default), 3h, and 6h	CP-1H CP-2H CP-3H CP-6H
Maximum Downdraft Height	Compares the effect of the maximum downdraft height, being 0.25, 0.35, and 0.50	CP-D025 CP-D035 CP-D050
Resolution Experiment	Evaluate the resolution effect on the results, degrading it into 60 km and enhancing it into 15 km	CP-15km CP-30km (Control) CP-60km
Type of Initial Condition	Changes the type of initial condition to be from the GFS model	CP-ERA5 (Control) (CP-GFS)
Best Configuration Test	A run with 2 changes inside the cold pool parameters	CP-1HD050 CP-1HD05015km

Source: Made by the author (2025).

The “ID” column serves as a reference for the names of the experiments. It is important to note that in the results, CP-ON represents the default configuration. In the sensitivity analyses conducted, the default values are specified in the labels. For instance, in the “Resolution Experiment,” the default configuration is set to a grid of 30 km (CP-30km), which is then changed to 60 km (CP-60km) and 15 km (CP-15km). To clarify, the following table emphasizes the default parameters:

Table 5.2 - Default values for the cold pool parameterization scheme

Parameter	Default value
Initial Condition Day	July 3rd, 2024
Cold Pool Lifetime	2 h
Maximum Downdraft Height	0.35
Resolution Experiment	30 km horizontal grid
Type of initial condition	Coming from ERA5

Source: Made by the author (2025).

We investigate the impact of cold pools by enabling (CP-ON) and disabling (CP-OFF) the parameterization, with CP-OFF serving as the control experiment in this case. In the subsequent rows, we conducted a sensitivity analysis on the parameters within the parameterization. Now our control experiment is the CP-ON configuration, with the Table 5.2 parameters. For the “Initial Condition Day” experiment, we varied the initial integration times: June 29 (00 UTC), 2024; July 1 (00 UTC), 2024; and July 2 (12 UTC), 2024 - comparing them with the default time. These periods were selected because they correspond to key moments in the storm’s evolution: shortly after HB was classified as a tropical storm, one day before it reached Category 5, and the day it reached Category 5, respectively.

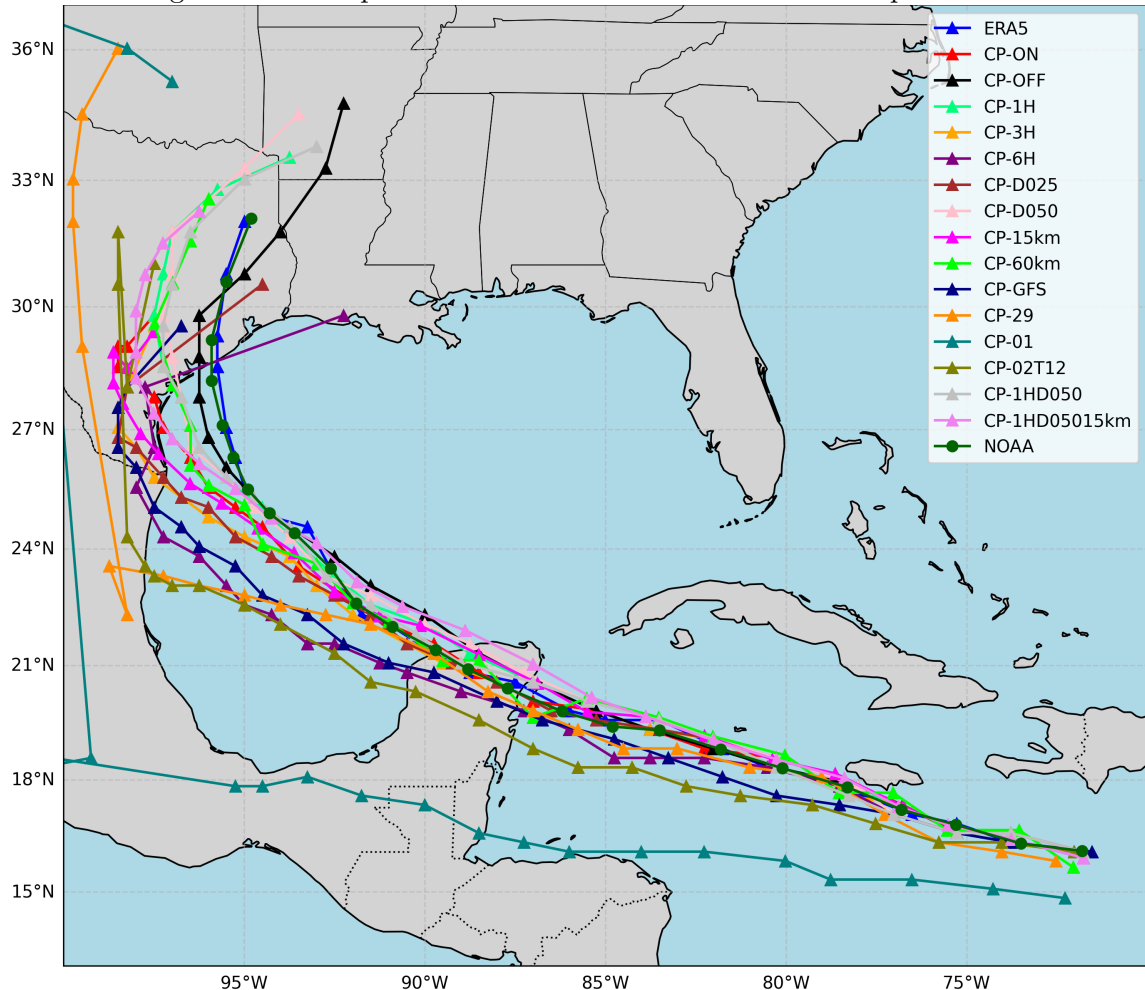
The “Cold Pool Lifetime” was adjusted from the default to durations of 1 hour, 3 hours, and 6 hours. The height of the mass flux above the surface is described by a parabolic function, and the coefficient of this function can be manipulated to alter the maximum height, with lower (higher) values indicating proximity (distance) to the surface. The “Type of Initial Condition” was switched from ERA5 to GFS, both initialized on July 3 (00 UTC), 2024.

During the computation of the initial 13 experiments, we observed that setting the cold pool lifetime to 1 hour and adjusting the maximum downdraft height coefficient to 0.5 resulted in lower errors in the initial results. Consequently, we conducted the “Best Configuration Test” with these parameter adjustments and repeated this configuration at 15 km, bringing the total number of experiments to 15. The reference data here is the best track dataset, and hereafter this dataset will be referenced as “NOAA”.

Keeping this in mind, Figure 5.6 shows all the trajectories for the 15 experiments, plus ERA5 and the reference best-track dataset.

As one can see in Figure 5.6, the numerous experiments clutter the scene and make visual comparison difficult. But one could notice the deviation of CP-6H and CP-01, which could

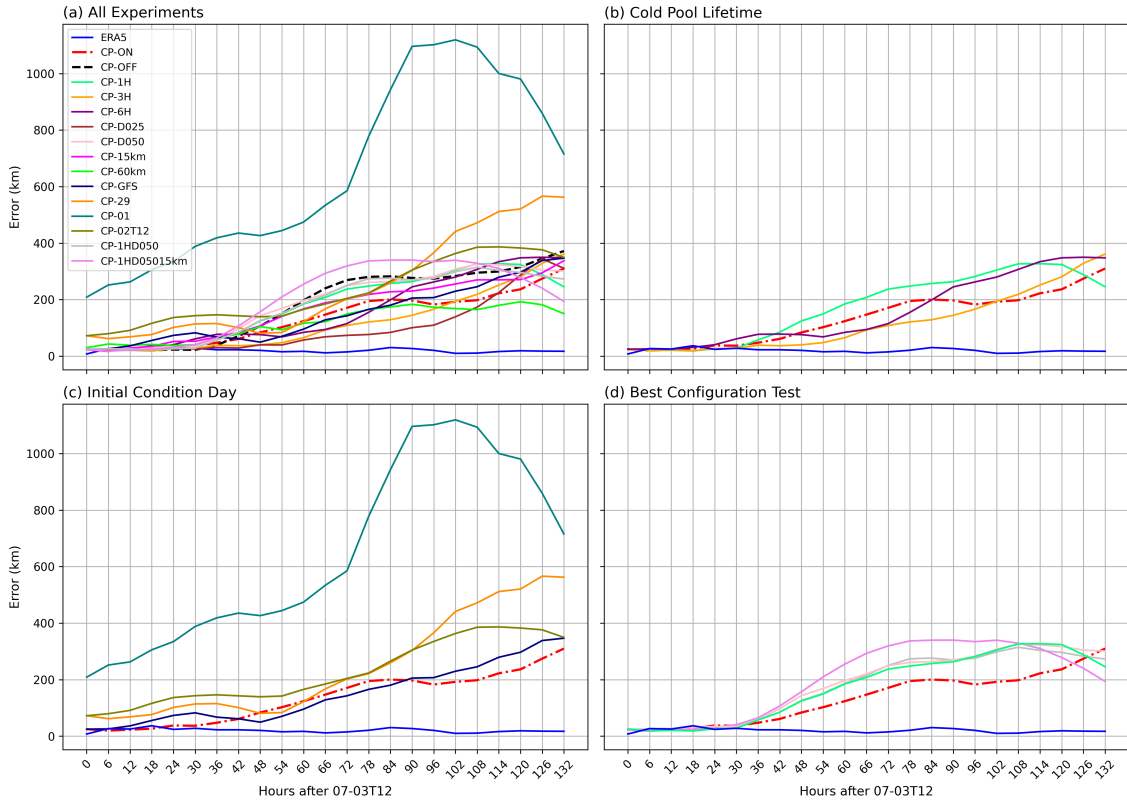
Figure 5.6 - Comparison of Storm Tracks Across All 15 Experiments



Source: Made by the author (2025).

be candidates to be withdrawn. To better visualize the difference between the trajectories, the distance between each trajectory and the reference data (NOAA's best track) was computed and shown in Figure 5.7.

Figure 5.7 - Errors (distance) between the trajectories



Source: Made by the author (2025).

It can be confirmed that CP-01 deviates significantly from the expected trajectory. Additionally, CP-6H offer limited discussion, as it is quite similar to the other experiments within their group. In Figure 5.7 (d), CP-1HD05015km does not show a significant improvement and will consequently be withdrawn. We will retain CP-1HD050 to seek the effects related to this configuration in the context of other aspects of tropical cyclones.

To summarize the experiments we intend to keep, a new table has been created, similar to Table 5.1.

Table 5.3 - Selected experiments

Parameter	Description	ID
Cold Pool Effect	Turn on and off the cold pool parameterization scheme	CP-ON CP-OFF (Control)
Initial Condition	Compares the effect of two initial conditions, June 29, July 2nd (noon), and July 3rd. Tested with 1st July	CP-29 CP-02T12 CP-03 (Control)
Cold Pool Lifetime	Compares the effect of cold pool life time being 1h, 2h (default), 3h, and 6h	CP-1H CP-2H (Control) CP-3H
Maximum Downdraft Height	Compares the effect of the maximum downdraft height, being 0.25, 0.35, and 0.50	CP-D025 CP-D035 (Control) CP-D050
Resolution Experiment	Evaluate the resolution effect on the results, degrading it into 60 km and enhancing it into 15 km	CP-15km CP-30km (Control) CP-60km
Type of Initial Condition	Changes the type of initial condition to be from the GFS model	CP-ERA5 (Control) (CP-GFS)
Best Configuration Test	A run with 2 changes inside the cold pool parameters	CP-1HD050

Source: Made by the author (2025).

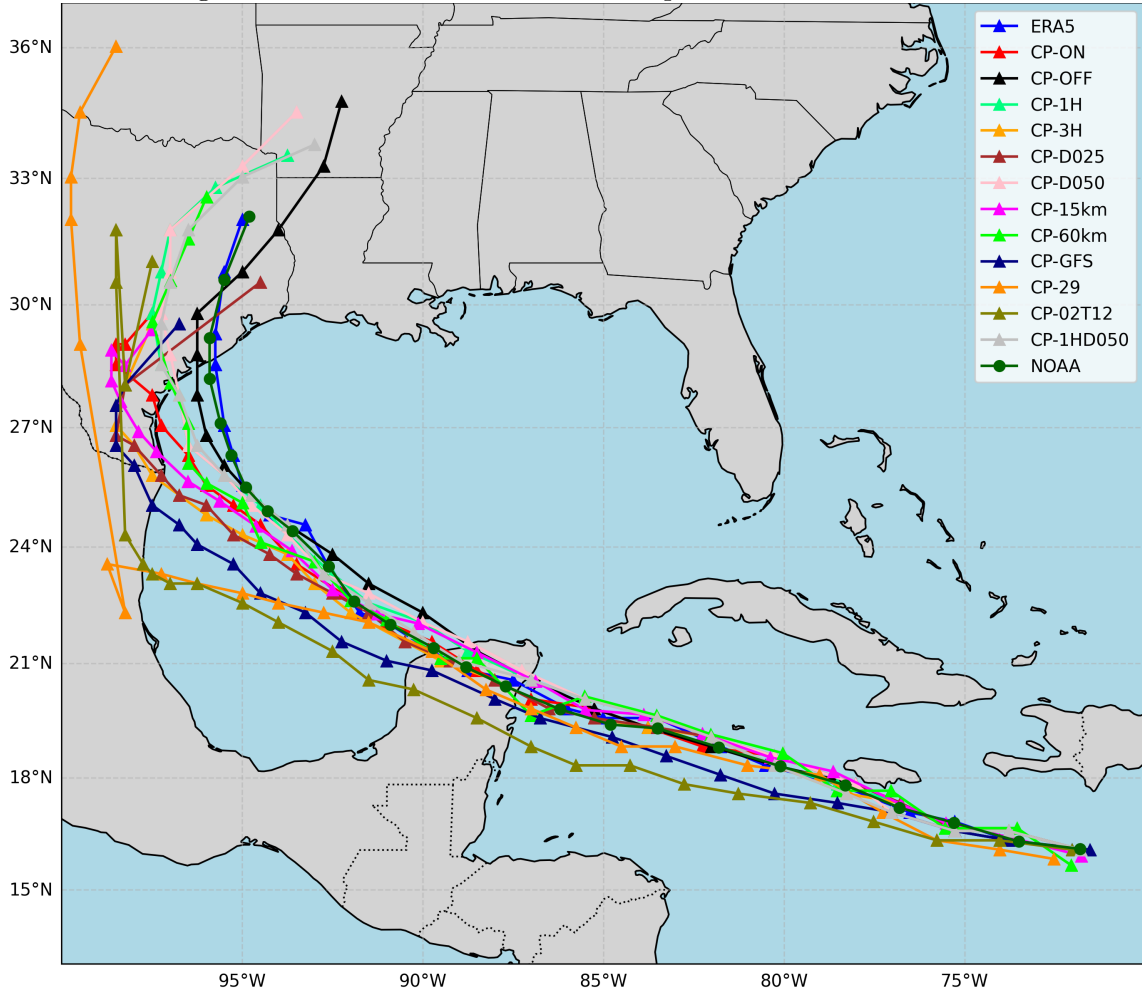
In the following subsection we will continue the results now keeping in mind the experiments listed at Table 5.3.

### 5.2.1 Trajectory

All trajectories are displayed in the Figure 5.8. The trajectories of each group of the Table 5.3 can be found at Appendix B.

This figure presents a map generated utilizing a tracking algorithm developed by the author. Firstly, the algorithm extracts each point corresponding to the minimum central pressure from the best track data between July 3rd and July 9th, 2024, sweeping a total integration period of 144 hours, with data plotted at 6-hour intervals. Furthermore, the minimum Mean Sea Level Pressure (MSLP) of the MONAN's forecast and ERA5 reanalysis is extracted within a predefined spatial box surrounding the best track minimum central pressure. For instance, the initial bullet point depicted in dark green (representing NOAA's best track at approximately 72.5° W) corresponds to the minimum central pressure obtained with the best track on July 3rd (00 UTC), 2024, while the final bullet point in dark green represents the data from July 9th (00 UTC), 2024 (close to 95° W).

Figure 5.8 - All tracks with selected experiments from Table 5.3



Source: Made by the author (2025).

At first glance, the reader will notice the observed congruence between the ERA5 reanalysis data and the best track observations. This strong agreement may be attributable to the reanalysis nature (Dulac et al., 2023), which integrates observational datasets throughout the integration period, thereby leading to this expected behaviour.

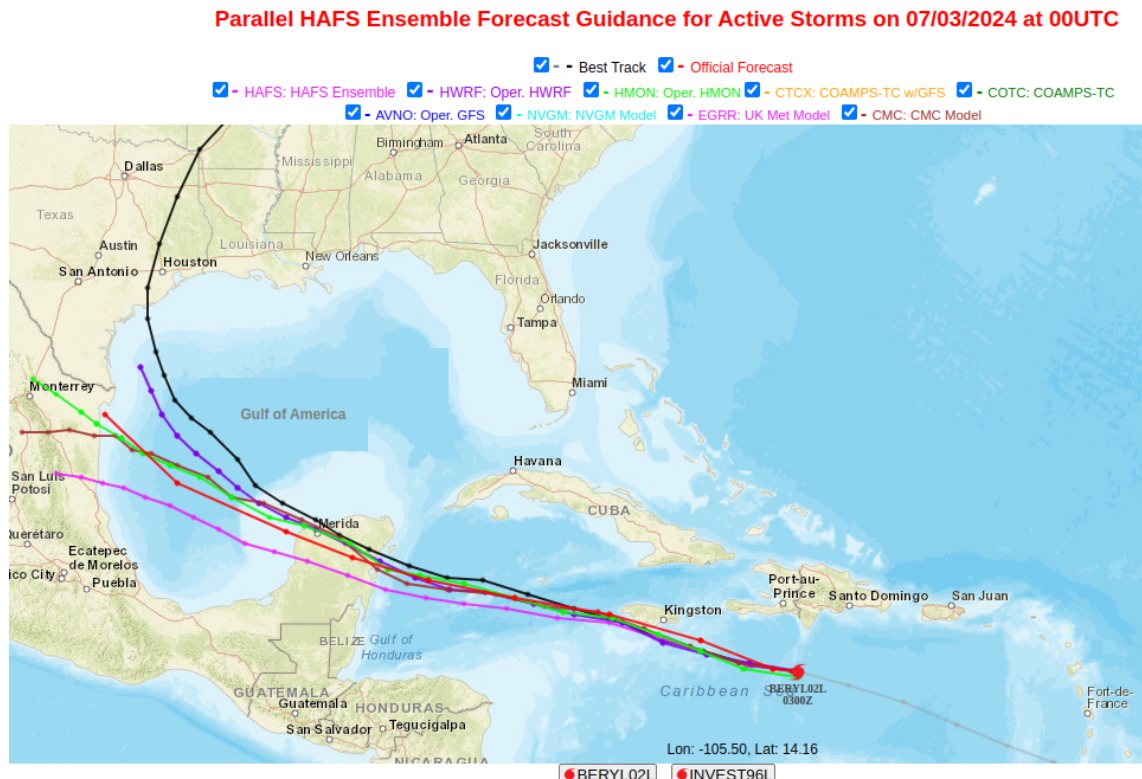
The CP-ON and CP-OFF experimental configurations exhibit comparable results for the majority of the integration period, with pronounced discrepancies evident near the Texas landfall and around the Yucatán Peninsula. A more detailed examination of these differences is warranted with other metrics. Concerning the cold pool lifetime, a 3-hour interval significantly deteriorates the accuracy of the forecasts. Furthermore, the downdraft maximum height coefficient of 0.50 appears to yield less precise results relative to the default values of 0.35 and 0.25. The trajectory forecasts utilizing a 60 km horizontal resolution

demonstrate closer alignment with the reference data, outperforming the 15 km and 30 km horizontal resolutions, with the 60 km configuration exhibiting superior performance. Additionally, forecasts initialized with the GFS (CP-GFS) model appear to underperform in comparison to those initialized with ERA5.

It is observed that when initialization occurs before July 3rd (00 UTC), 2024, a visible degradation in trajectory forecast accuracy ensues. Note that there is a tendency for earlier initialization to result in poorer forecasts, a fact that can be confirmed later on with the MAE and RMSE metrics. This underscores the necessity of incorporating a module within the model to assess ensembles of initial conditions, also in agreement with what is found in the literature (DONKIN; ABIODUN, 2023).

Finally, the configuration incorporating two parameters that have been changed simultaneously does not reveal significant deviations from the default setup. Overall, the forecasts exhibit a westward bias, a phenomenon that is also apparent in forecasts issued by the Hurricane Analysis and Forecast System (HAFS), as shown at Figure 5.9.

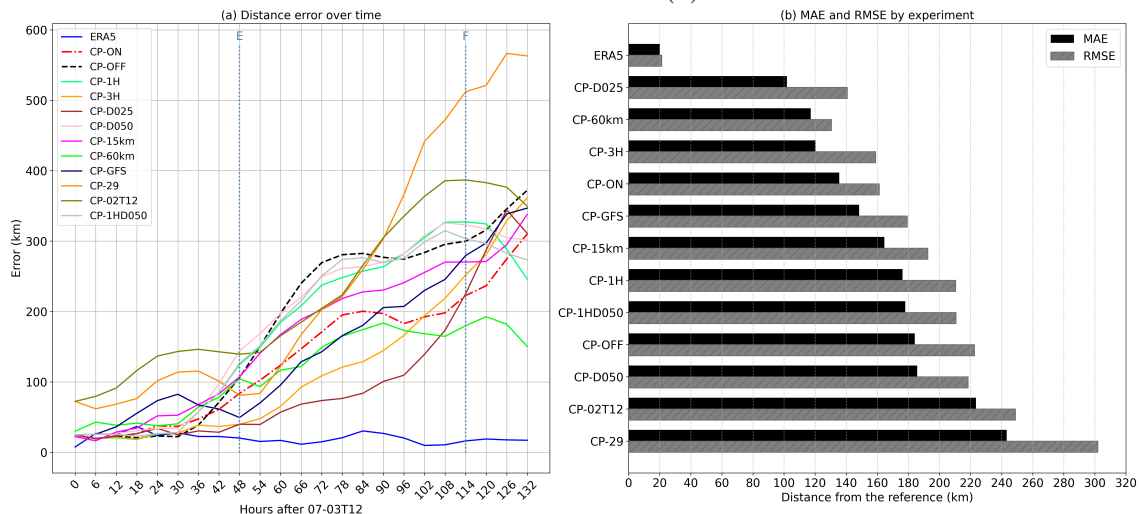
Figure 5.9 - Forecast made for Hurricane Beryl starting at July 3rd (00 UTC), 2024, available at the HAFS website



Source: <<https://www.emc.ncep.noaa.gov/HAFS/HAFSEPS/index.php>> .

The next panel provides complementary information to the analysis, now in a more quantitative manner. It is important to mention that the time series display the errors after 12h of spin-up, and that value is maintained and the further analysis. In Figure (a), it is possible to better distinguish the differences among the experiments over time. In other words, it shows when each experiment presents lower errors throughout the integration period, along with an initial comparison among them. It is important to note that the vertical line E indicates the moment the hurricane makes landfall on the Yucatan Peninsula, while the vertical line F marks its entry into Texas. In Figure (b), this comparison becomes even clearer, especially because the bars are arranged vertically from the lowest to the highest error (from top to bottom).

Figure 5.10 - Track errors of the MONAN forecast and ERA5 reanalysis with the best track as reference. 12 hours of model spin-up are withdrawn from the analysis. (a) is displayed the distance error computed as the great circle, and (b), the MAE and RMSE calculated from (a).



Source: Made by the author, (2025).

As shown in the previous figure, ERA5 delivers the best track prediction performance. This could be attributed to the fact that ERA5 is a reanalysis product, meaning that observational data assimilation is injected into the model at each integration step. A fairer comparison would require conducting this analysis with another model similar to MONAN, which will be left for future work.

Overall, forecasts tend to show errors below 100 km up to 42 hours of lead time, except for those initialized earlier (CP-29 and CP-02T12). After 60 hours of forecast (two and a half days), some experiments begin to exceed 200 km of error. However, cold pool influence on track prediction only reaches this threshold after 84 hours (three and a half days), and

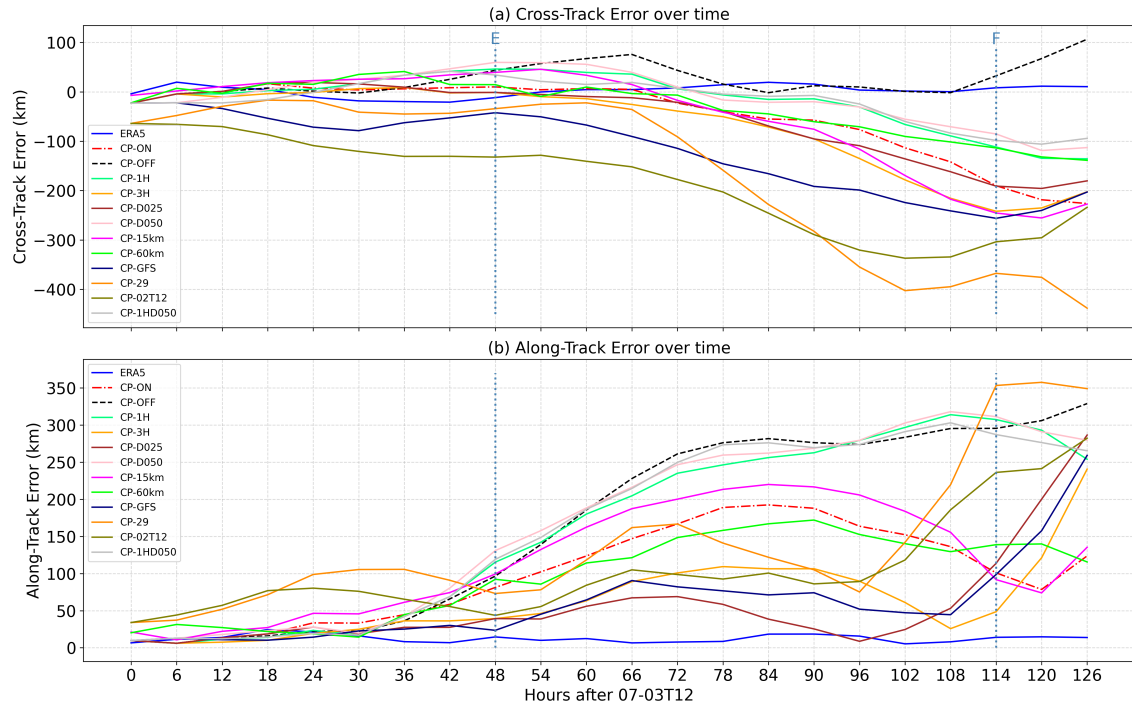
the CP-D025 experiment only reaches it after about 111 hours (four and a half days). Therefore, we observe that with cold pool parameterization, forecast skill is extended by up to two days compared to the configuration without this scheme, for this specific case study.

In the literature, the best forecast limit reported is around 120 hours (five days) (ZHOU; TOTH, 2020), (SIPPEL et al., 2022). It is worth emphasizing that forecast errors beyond this threshold should be considered “chaotic,” given the nonlinear nature of the system.

The computation of MAE and RMSE provides insights into the overall error behavior in track forecasts. While MAE offers a generalized view of the error, RMSE takes into account the squared deviations, assigning more weight to larger errors at each time step. In general, it is notable that simply enabling the cold pool parameterization (CP-ON) already improved the track forecast, reducing the MAE by approximately 22% compared to CP-OFF. Furthermore, we observe that tuning the parameters, such as in CP-D025, CP-3H, and modifying the resolution to 60 km (CP-60km), further enhanced this performance.

By observing the Figure 5.9 and Figure 5.10, one could notice the westward deviation in the forecast. The next panel showing the CTE and ATE can confirm this behaviour, at Figure 5.11.

Figure 5.11 - CTE (a) and ATE (b).



Source: Made by the author, (2025).

Overall, most of the forecasts show a negative CTE, meaning there is a leftward (westward) deviation from the observed trajectory, confirming Figure 5.8, which displays all the tracks, and Figure 5.9. This trend is particularly clear in the CP-02T12 experiment. Since the first hour of the forecast, the CTE is negative, which aligns with the fact that the predicted trajectory is consistently to the left of the observed one.

It is interesting to note that the CTE behavior differs significantly between the CP-ON and CP-OFF experiments. While CP-OFF maintains a positive CTE, CP-ON gradually shifts to a negative CTE as the integration period progresses. Notably, CP-ON begins to deviate leftward after around 72 hours of integration, after passing through the Yucatan Peninsula, whereas in other experiments, such as CP-OFF and CP-D025, this deviation occurs earlier.

Interestingly, despite exhibiting large overall errors (Figure 5.10), the CP-D050 experiment performs better than CP-ON in this metric, as it does not deviate as strongly. This highlights the importance of evaluating forecast performance from multiple perspectives and understanding the sources of these differences, which we will further investigate using meteorological fields.

This westward bias was also noted in the forecasts from both the HAFS (Figure 5.9) and the UK Met Office (Figure 5.12) for Hurricane Beryl.

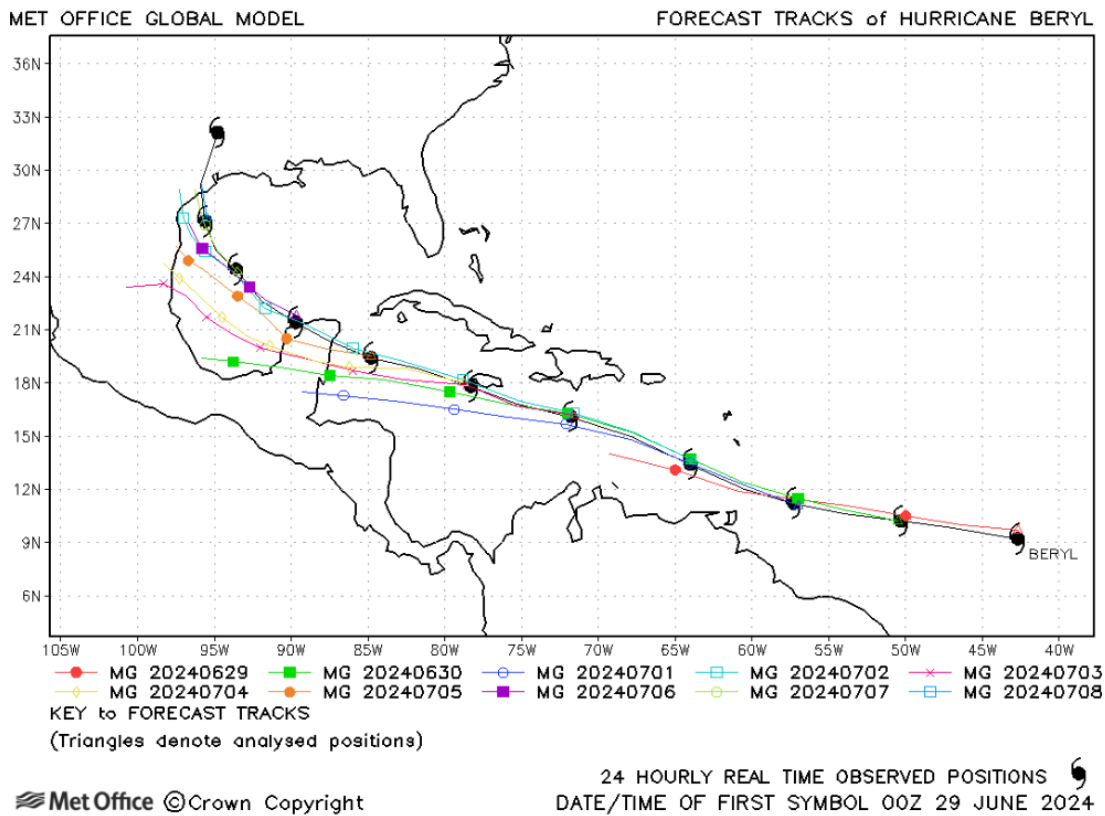
The report ([Met Office, 2024](#)) indicates that the track was forecasted with a notable degree of accuracy throughout the Caribbean region, furthermore, it was observed that there was a left-of-track bias in the forecasts as Beryl progressed into the Gulf of Mexico.

In general, the ATE is positive across all experiments, indicating a consistent tendency for the MONAN model to move faster than observed. Note that ERA5 also displays this trend, though it is not as pronounced as in MONAN.

When comparing CP-ON and CP-OFF, a growing ATE trend is evident in CP-OFF. As the integration period increases, CP-OFF moves increasingly ahead of the observed track, reaching 225 km ahead at 66 hours, whereas CP-ON is only about 150 km ahead at the same time.

The CP-D025 experiment appears to be more in phase with the observations in this metric than CP-ON during most of the forecast period, despite having a greater leftward deviation compared to CP-ON. Despite larger errors in track positioning, the early-initialized forecasts manage to better match the best track in terms of propagation speed. In this case, the forecast initialized with GFS outperformed the forecast initialized with ERA5 during most of the integration period.

Figure 5.12 - Tracking available by the UK Met Office.



Source: <<https://www.metoffice.gov.uk/research/weather/tropical-cyclones/verification/seasons/nhem2024.>>

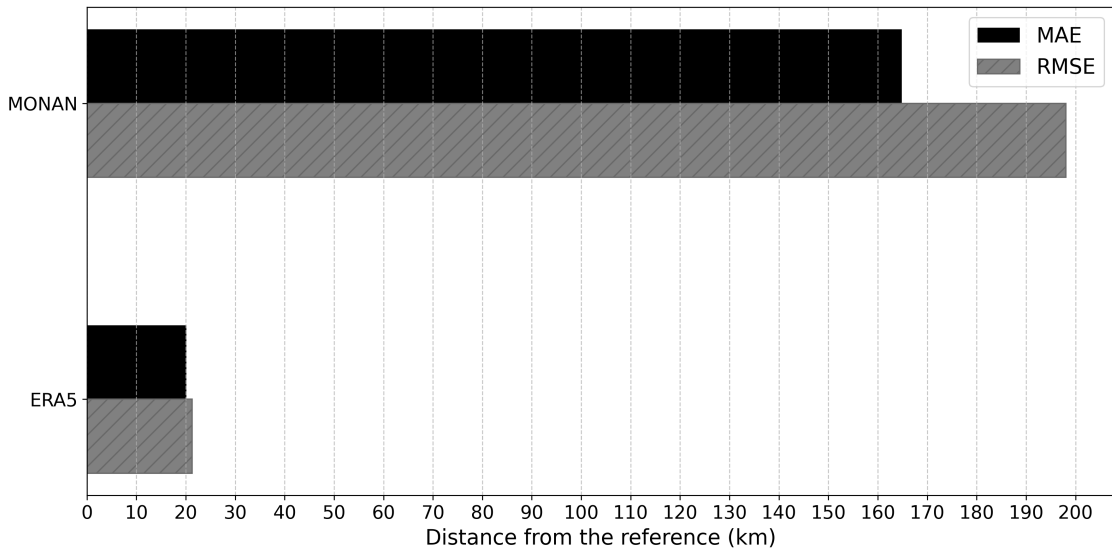
A mean error performance of all MONAN forecasts were computed and shown at Figure 5.14.

In general, the MONAN forecast is approximately 8 times greater than the ERA5 reanalysis. Again, we can infer that it is not a fair comparison between the MONAN forecast and the ERA5 reanalysis, but it is important to notice the error scale to give us insights about improving the MONAN forecast.

### 5.2.2 Intensity

The minimum MSLP found in the track and best track was plotted as Central Pressure in Figure 5.14 (a). The forecasted wind at the first model level alongside with the maximum wind speed of best track and the 10 meters instantaneous gust-front of ERA5 are displayed in Figure 5.14 (b). The Saffir-Simpson wind scale is denoted by black lines to guide the reader in the forecast scale.

Figure 5.13 - Overall performance of MONAN trajectory forecasts compared with ERA5 reanalysis.



Source: Made by the author (2025).

In general, this panel indicates that the ERA5 reanalysis demonstrates poorer performance in predicting central pressure compared to MONAN forecasts. This finding aligns with the work of Dulac et al. (2024), who highlight that inaccuracies in central pressure estimations can lead to underestimations in wind speed intensity predictions. Given that MONAN is initialized with ERA5 reanalysis fields, it is anticipated that the initial conditions also carry those uncertainties.

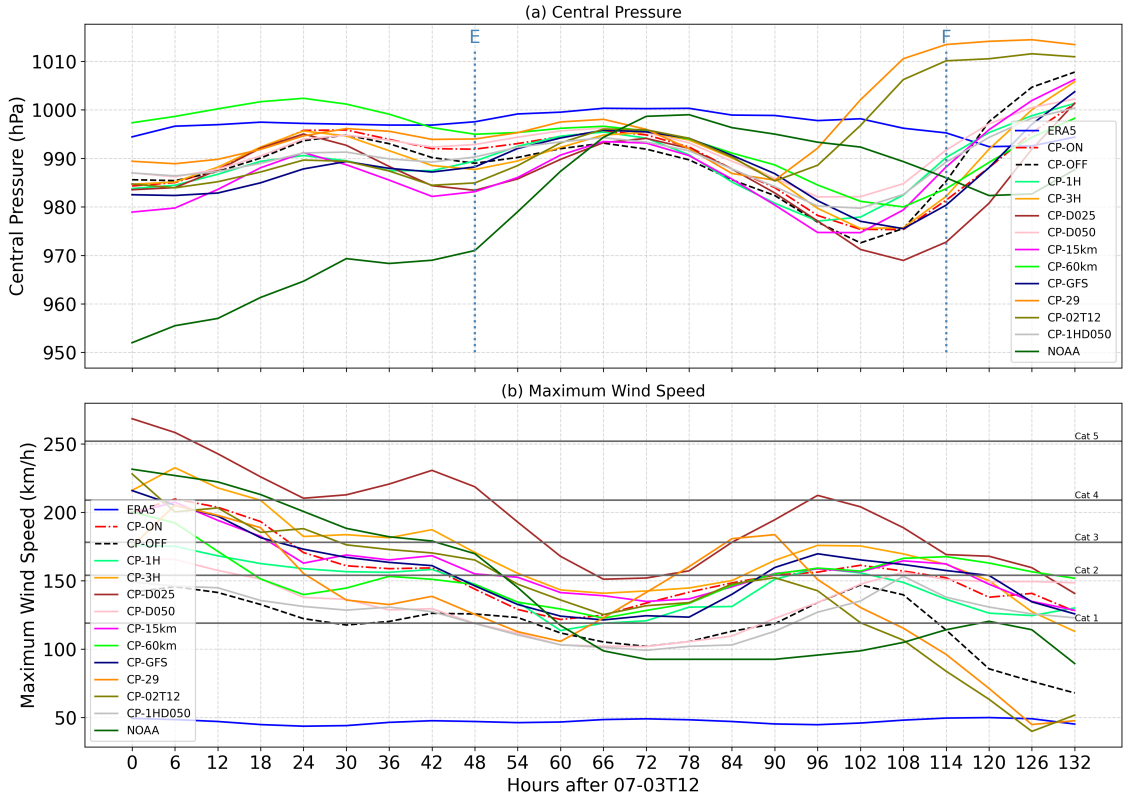
As shown in Figure 5.14 (a), the MONAN forecasts exhibit a similar trend; however, there are notable outliers, particularly in the CP-29 and CP-02T12 experiments, especially following the Texas entrance (marked by the vertical line "F").

The initial high-pressure peak occurring between 24 and 30 hours of the forecast is in phase with the best track. However, after the passage of the Yucatan Peninsula, at 66-72 hours of forecast, the experiments fall out of phase by approximately 6 hours, with MONAN displaying an earlier peak than the best track. A forecasted low-pressure system intensifies around 102-108 hours, while the best track identifies this feature closer to 126 hours. This behavior is consistent with what the ATE indicated earlier.

The cold pool effect is most noticeable in Figure 5.14 (b). The CP-ON configuration tends to generate more wind than CP-OFF, yet it does not reach the strength reported in the best track data.

The forecasts initialized earlier than the standard (CP-29 and CP-02T12) in Figure 5.14 (b)

Figure 5.14 - Comparison of Forecasted and Observed Central Pressure and Wind Speeds for Hurricane Beryl. Here, a 12-hour model spin-up was also withdrawn, starting the time series on July 3rd, 12 UTC.



Source: Made by the author (2025).

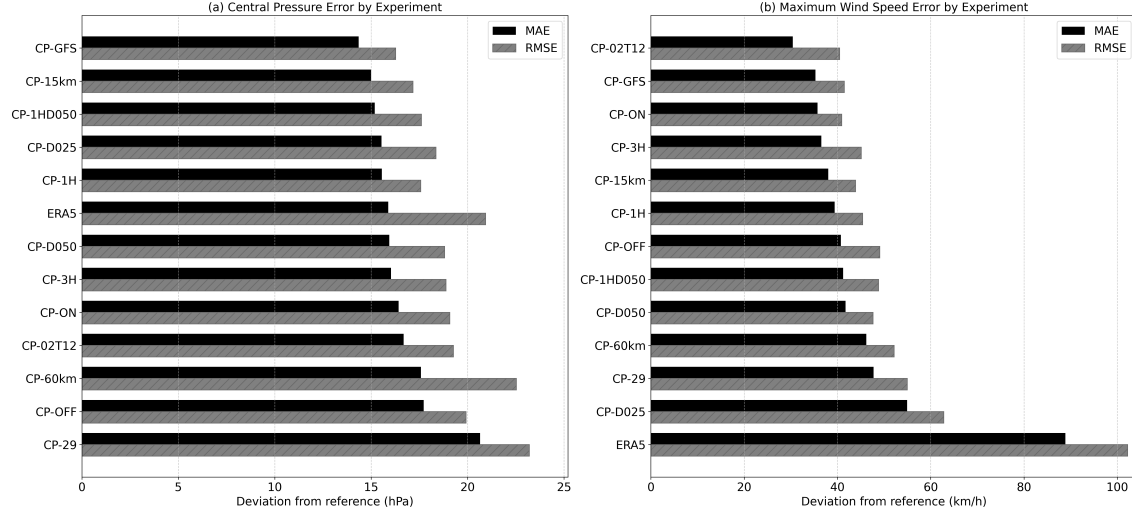
also emerge as outliers. This discrepancy becomes particularly evident when we examine the last intensification moment from the best track, at 120 hours, achieving Category 1. In contrast, these forecasts peak at 90 hours, showing even greater intensity as they reach Categories 2 and 3. This indicates a significant divergence of a full day between these forecasts and the intensity described by the best track. This trend, consistent with the observations in the ATE, is also reflected in the other forecasts. Furthermore, the anticipation of peak intensity worsens as the integration time extends.

One of the most striking forecasts in this figure is from the CP-D025 experiment, which illustrates an excessively intense system. This intensity arises because the mass flux is situated much closer to the surface compared to the other experiments, resulting in stronger downdrafts and, consequently, a more intense gust.

The panel presents a quantitative evaluation of the forecasts and ERA5 reanalysis in comparison to the intensity observed in the best track. The RMSE in these figures is a particularly insightful metric due to the oscillatory nature of the event, as this error is

computed as a weighted average of the squared differences.

Figure 5.15 - Central Pressure and Maximum Wind Speed Errors.



Source: Made by the author (2025).

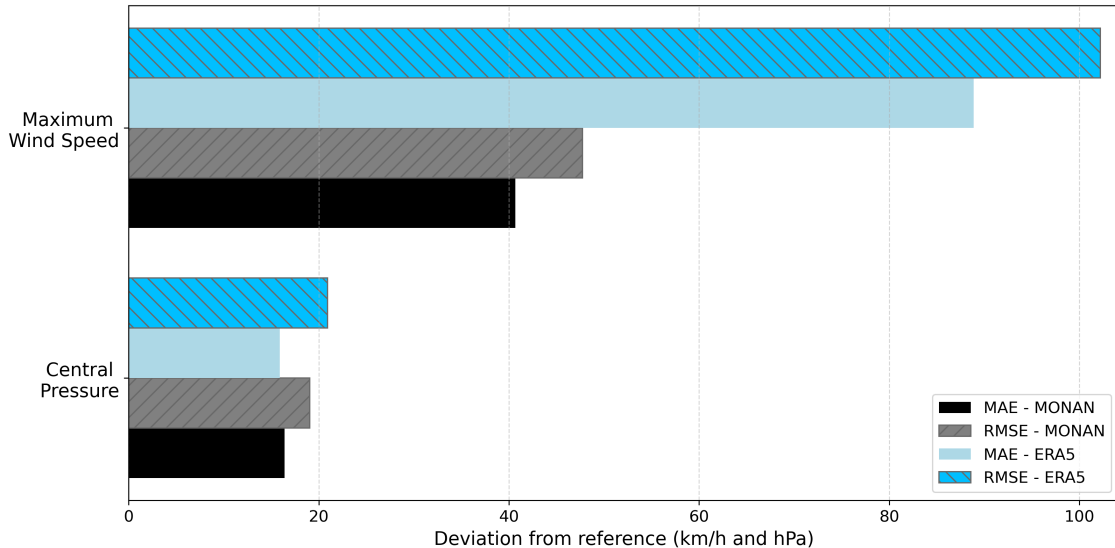
In Figure 5.15 (a), the performance of the cold pools in the pressure field is evident, with CP-ON showing a reduction in MAE of approximately 8% compared to CP-OFF. Furthermore, the importance of investigating and tuning the parameters within this parametrization is highlighted, as modifying them leads to further improvements in pressure representation. Notably, the CP-1HD050 configuration stands out, despite not achieving the same improvement in the wind field. This relationship between cold pools and the pressure field could be further explored in future studies.

In Figure 5.15 (b), it is interesting to note that CP-ON reduces the MAE by approximately 12.5% compared to CP-OFF, while the RMSE shows an even greater reduction of about 20%. Although the CP-D025 experiment produces a system that is too intense, diverging from the best track, as shown in the previous figure, it does not result in a worsening of the pressure field, once again underscoring the importance of parameter tuning within the convection scheme.

By the end, a mean of Figure 5.16 is presented next, to highlight the differences between ERA5 and MONAN.

In contrast to the trajectory analysis, the advancements in the forecasting capabilities of MONAN are evident, particularly in the substantial reduction of maximum wind speed, which has decreased by approximately 54% when compared to the ERA5 reanalysis.

Figure 5.16 - Central Pressure and Maximum Wind Speed errors by MONAN compared to ERA5.



Source: Made by the author (2025).

### 5.2.3 Rainfall

In this subsection, we will analyze the rainfall through three perspectives: the rainfall pattern and spatial distribution; the mean and distribution of rain volume; and the extreme values.

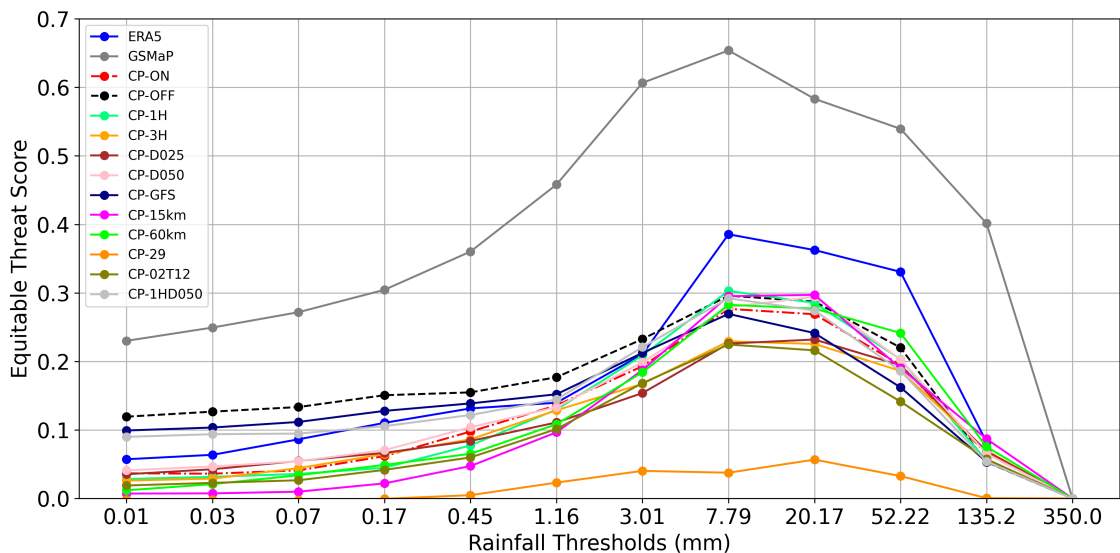
#### 5.2.3.1 Pattern and spatial rainfall distribution

Following the workflow proposed in the Metrics section, we can quantify the spatial distribution of rainfall using the ETS and Pearson correlation coefficient. This analysis focuses on a specific area ( $106\text{--}51^{\circ}\text{W}$ ,  $10\text{--}41^{\circ}\text{N}$ ) over a six-day forecast period, from July 3rd to July 9th (00 UTC). Upon reviewing the literature (MARCHOK et al., 2007), (BRACKINS; KALYANAPU, 2020), (LUITEL et al., 2018), we found that these metrics are influenced by the forecasted track and are typically calculated over a defined region, usually a 500-600 km radius around the best track trajectory, rather than the broader area we are examining. In their 2007 study, Marchok et al. discuss this in detail and suggest potential improvements to compute those metrics, also regarding resolution dependencies. We opted to calculate the accumulated area to reduce the track error effect, though it is important to note that this approach may also capture local rainfall accumulations. In our study area, identifying the hurricane is relatively straightforward; for example, reports indicate that Beryl produced 13.2 inches (approximately 335 mm) of accumulated rainfall over Jamaica (LI et al., 2025), so because of this, the broader area should not be this much of

a problem, but meant to be a simple view of the spatial rainfall distribution. For future work, we propose adapting the previous approach to more accurately represent both the ETS and Pearson correlation coefficients.

Figure 5.17 illustrates the ETS for various rainfall thresholds (in mm). These thresholds were determined using a log distribution, similar to the method presented by Marchok et al. in 2007. The maximum threshold was established with consideration of the maximum distribution observed in the datasets<sup>2</sup>. For instance, the maximum accumulated rainfall measured was 252.5 mm, 252.0 mm, 453.7 mm, 485.4 mm, 359.6 mm for GPM-IMERG, ERA5, GSMAp, CP-ON, CP-OFF, respectively.

Figure 5.17 - Equitable Threat Score for all experiments, ERA5 dataset and GSMAp dataset.



Source: Made by the author (2025).

The GSMAp exhibits the best score due to its nature as a satellite-based system. It is important to highlight that for this and other analyses, both GSMAp, ERA5, and GPM-IMERG data were downsampled to the model's resolution of 30 km. In the case of GSMAp, the resolution was reduced from 4 km to 30 km. The further analysis will explicitly mention this whenever the data is not downsampled.

ERA5 shows better agreement in the moderate to extreme rainfall range (between 3 and 135 mm), but it is important to note that the maximum rainfall is relatively low compared to GPM-IMERG. Thus, ERA5 does not score well regarding rainfall data produced by this

<sup>2</sup>The Python function used was: `numpy.logspace(numpy.log10(0.01), numpy.log10(350), num=12)`

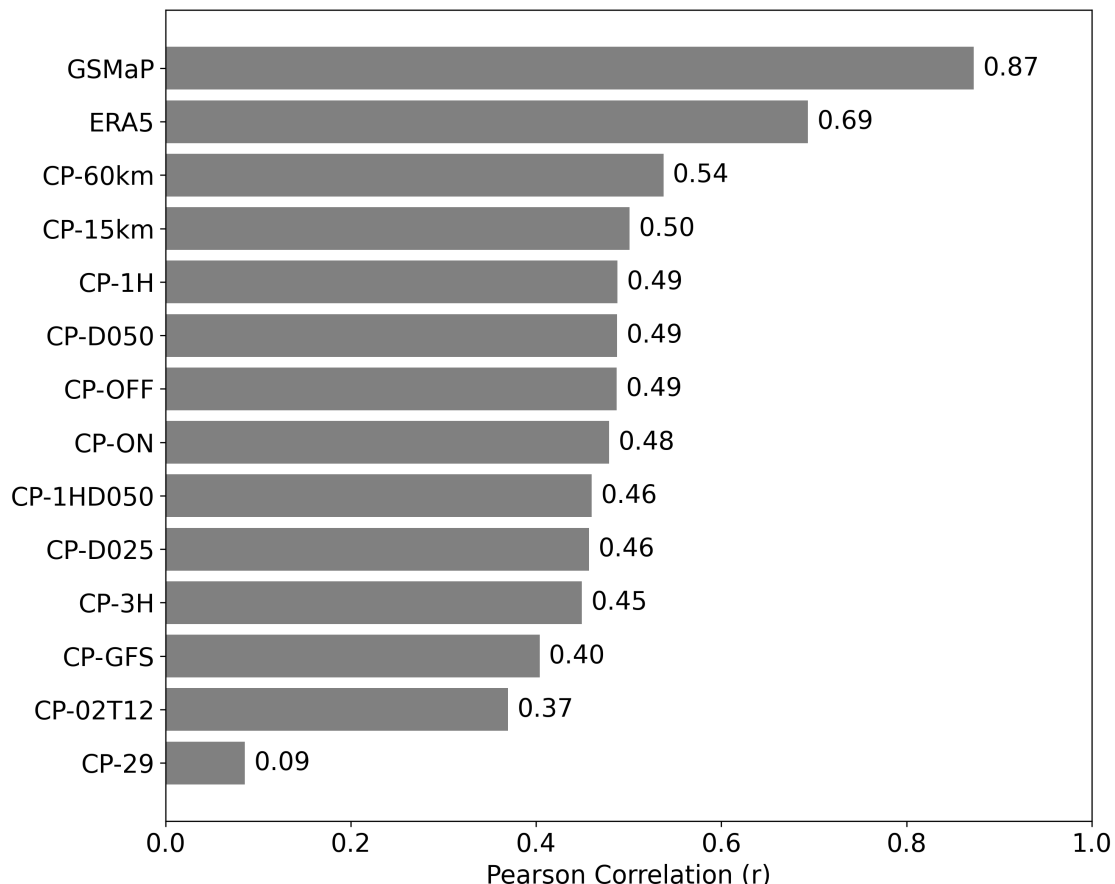
event.

In general, the forecasts from MONAN display similar behavior, with some outliers. For example, CP-OFF shows a better score at the lower thresholds compared to other forecasts, meaning that local rainfall is slightly better in agreement with the observed data, but it displays the same trend in the extreme thresholds. Another outlier is CP-29, which exhibits poor agreement with the observed data, especially due to a poor predicted trajectory.

At more extreme thresholds (above 135 mm), the scores for all data types drop significantly, indicating the need for further investigation into this topic.

The Pearson correlation coefficient is shown next, in Figure XXX. This coefficient was calculated across the entirety of the spatial domain, indicating that it provides a correlation value representative of the entire scene.

Figure 5.18 - Spatially averaged Pearson correlation coefficient over the entire domain



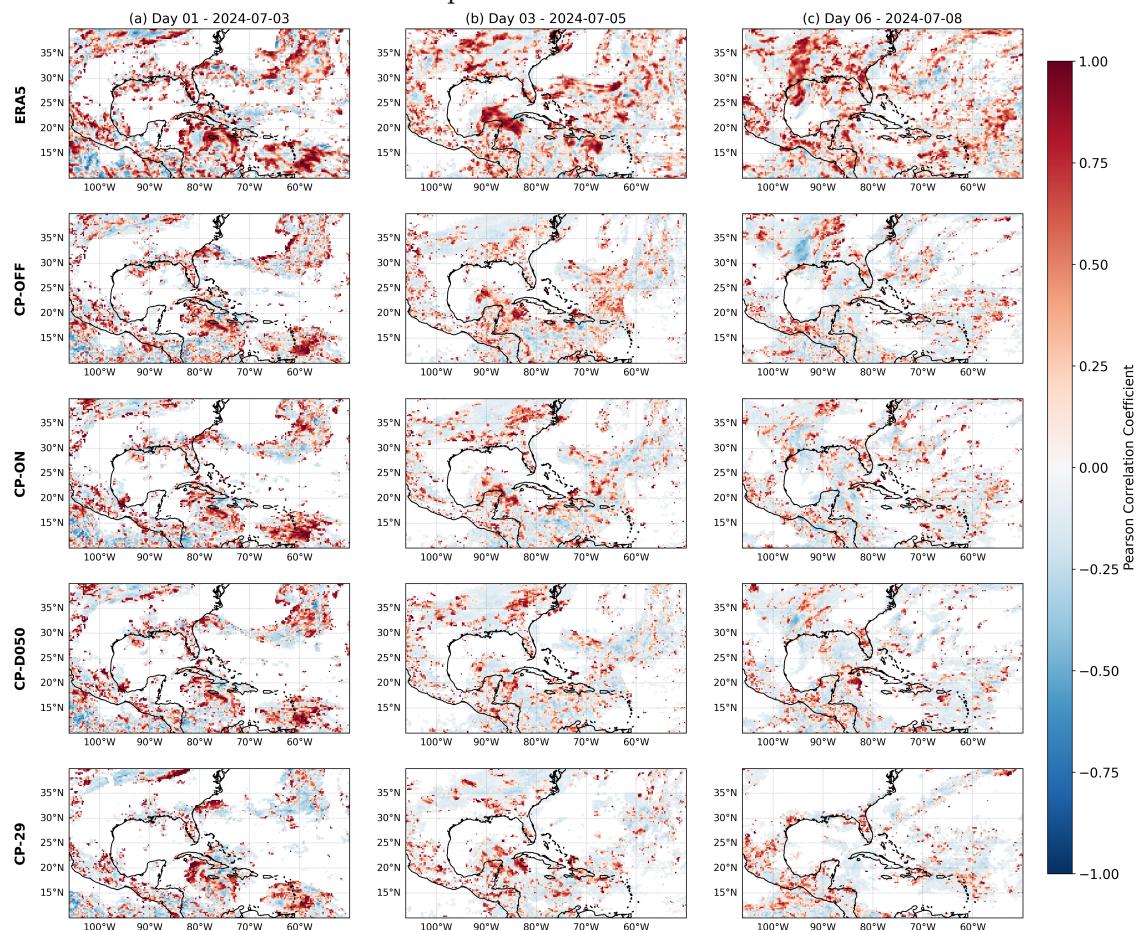
Source: Made by the author (2025).

Once again, the data from GSMAp and ERA5 stand out with the strongest correlations with GPM-IMERG. Interestingly, this highlights the effects that changes in resolution can have, as seen more clearly in the panel of Figure 5.19.

Regarding the forecasts from MONAN, the average correlation is around moderate, excluding outliers such as GFS, CP-29, and CP-02T12. Note that for the last two forecasts, the bias from the trajectory itself strongly influences the calculation of this metric, as CP-29 and CP-02T12 also had the largest tracking errors (Figure 5.10).

To better infer the locations with the best/worst correlations, as well as to gain a clearer understanding of the temporal evolution of correlation in the forecasts, Figure 5.19 displays the correlation spatially, computed from daily rainfall accumulations.

Figure 5.19 - Spatial distribution of daily Pearson correlation values to assess temporal evolution of forecast performance



Source: Made by the author (2025).

In this figure, the selected days represent: (a) the starting point of forecasts, immediately following the weakening of Hurricane Beryl, but corresponding to the highest observed rainfall (over Jamaica); (b) its passage over the Yucatán Peninsula, during which the hurricane weakens from Category 1 to a tropical storm; and (c) landfall in Texas on the North American continent. It is important to note that each column represents the accumulated rainfall for 24 hours; thus, panel (a) corresponds to rainfall accumulated over July 3rd, and so on.

The top row presents correlation values derived from ERA5 reanalysis, which exhibited strong correlations, while the bottom row shows the correlation from the CP-29 forecast, which had the weakest agreement. To evaluate the effect of cold pool parameterization, CP-ON and CP-OFF are aligned for comparison. Additionally, CP-D050 was selected as an example of moderate correlation to identify where the internal parameterization settings are influencing correlation variability. Other experiments referenced in the study are presented in the appendix.

Regarding the temporal evolution of correlation, a general degradation in forecast performance over time is observed, with the reanalysis data maintaining higher consistency, as expected. Notably, CP-29 shows a significantly sharper decline in correlation over time compared to CP-ON, for instance.

For instance, CP-29 reveals a pronounced track error upon landfall in Texas ( $100\text{--}90^\circ\text{W}$ ,  $25\text{--}35^\circ\text{N}$ ), as evidenced by a near-zero correlation in that region. In the same region, CP-D050 and CP-OFF present negative correlations when compared with CP-ON.

CP-D050 fails to represent rainfall over the Yucatán Peninsula, whereas CP-ON appears to generate more cohesive rainfall patterns than CP-OFF ( $20\text{--}25^\circ\text{N}$ ,  $90\text{--}80^\circ\text{W}$ ). Both CP-D050, CP-ON, and CP-OFF also show localized overestimation of rainfall east of Cuba, a region that does show rainfall in the ERA5 dataset.

Selected snapshots corresponding to these dates were chosen to confirm the previously discussed relationships. A panel displaying these time steps alongside IMERG and GSMAp (both downscaled to 30 km resolution) is presented in Figure 5.20.

One of the most notable aspects across the panels is the skill of the parameterizations in generating cohesive rainfall patterns (e.g., CP-ON and CP-GFS in column a), and in some cases, reproducing the hurricane's spiral structure (panel b—seen in CP-ON, CP-D050, and CP-GFS).

Regarding maximum and average rainfall, the forecasts tend to overestimate precipitation relative to observations. However, in column (b), both CP-ON and CP-D050 are close to approximating the rainfall amounts observed by GSMAp.

It is evident that these panels visually reflect the patterns observed in the cross-track and along-track errors, particularly in column (c). For example, the Hurricane Beryl location by GPM-IMERG is slightly different from CP-ON, since the CP-ON forecast is located farther north.

The bias computed against GPM-IMERG is presented in Figure 5.21. However, it is important to note that bias is not a particularly reliable metric for this type of phenomenon, as it is heavily influenced by trajectory errors inherent to tropical cyclone forecasts.

Using the same example as before, in column (c), a positive bias can be observed in the hurricane region, clearly indicating that the hurricane position produced by CP-ON is farther north compared to GPM-IMERG. Moreover, this figure reinforces the results shown previously with the cross- and along-track errors (Figure 5.10).

As previously discussed (Figures XXX and XXX), changing the horizontal resolution results in forecasts with good correlation. To further investigate this, Figure 5.22 presents forecasts at 15 km, 30 km, and 60 km horizontal resolution, using the same spatial and temporal domains as in Figure 5.20.

The 30 km forecast (CP-30km) performs notably well compared to ERA5 (with 25 km resolution) and GSMAp (4 km resolution), due to its ability to reproduce the spatial characteristics of rainfall seen in GPM-IMERG, especially the arc-shaped rainband observed in panel (a).

A clear gain in spatial detail and rainfall morphology is observed in the 15 km forecast. In particular, the clustering of rainfall and the reproduction of the hurricane's spiral bands stand out, further highlighting the effects of cold pools, features that have also been documented in the literature (SAKAEDA; TORRI, 2023), (FREITAS et al., 2024), (HAERTER et al., 2018), (FENG et al., 2015), (VOGEL et al., 2021). Interestingly, this rainfall clustering effect is also observed in the CP-60km experiment. Despite the loss of detail due to its coarser resolution, it still manages to capture the spiral structure (panel b) and localize regions of intense rainfall (panels a and c). A more detailed investigation (and confirmation) of the role of cold pool parametrization in cloud organization will be left for future work.

Finally, to specifically assess the morphological structure of the clouds, as well as the depth of the cloud tops being formed, the panels in Figure 5.23 were created. To isolate the influence of horizontal resolution, Figure 5.24 was also developed. Once again, these panels were constructed using the same spatial and temporal domains as Figures 5.20 and 5.22, but now with cloud-top temperature (i.e., brightness temperature) as the primary variable.

Naturally, the cold pool effect leads to deeper convection, which explains the rainfall values observed in Figures XXX and XXX. It is noteworthy that the cloud-top temperatures in the simulations are very close to those observed, particularly when the cold pool parametrization is active, such as in the CP-ON configuration. The CP-D050 forecast, which has a mass flux profile positioned farther from the surface, produces slightly deeper clouds. This is consistent with its higher cloud base, which results in taller cloud structures overall.

Spatially, cloud coverage in the CP-3H configuration is greater than in the others, due to the duration of the cold pool effect and its ability to continuously generate new cloud populations. In general, the forecasts manage to represent morphological characteristics, such as cloud size and extent, comparable to observations.

Now, when comparing different resolutions, it becomes clear that the spatial definition of hurricane structure is highly dependent on resolution. At 60 km, the hurricane center becomes nearly indistinguishable, and key structural features, such as the spiral bands, are either poorly resolved or completely absent. In contrast, simulations at 30 km closely resemble those at 15 km in several aspects. Both effectively capture the delineation of the rainbands and the overall spiral organization of the hurricane, with the 15 km forecast naturally providing more detail and sharper gradients. This underscores the significance of horizontal resolution in accurately representing fine-scale convective structures and highlights the threshold at which certain morphological characteristics begin to degrade markedly.

#### 5.2.3.2 Rainfall mean and overall distribution

For this subsection, two types of metrics were employed: Probability Density Functions (PDFs) and Cumulative Distribution Functions (CDFs). As previously mentioned (Section 4), empirical functions are computed, meaning that they are derived directly from the natural distribution of the data. To calculate these functions, a Python script was developed. First, hourly rainfall data over the entire duration of the event (6 days) were gathered. These data were then sorted into thresholds using a logarithmic scale, generating histograms for each experiment, as well as for the GPM-IMERG, ERA5, and GSMap datasets. Both the forecast and the dataset were at the same horizontal resolution of 30 km. Subsequently, the PDFs and CDFs were computed from these histograms. Note that these distributions are normalized according to the total number of data points. Figure XXX displays the computed PDFs in the first column (A, C, E), and the corresponding CDFs in the second column (B, D, F).

In Figure 5.25 A, ERA5 exhibits a trend similar to GPM-IMERG at lower thresholds but overestimates rainfall in the moderate range (above 1 mm/h), returning to a closer

match at higher thresholds, around 20 mm/h. In contrast, GSMAp generally overestimates rainfall at both low and moderate thresholds (up to 20 mm/h), and this overestimation becomes more pronounced at heavy rainfall, exceeding even the MONAN forecasts.

Regarding CP-ON and CP-OFF, both configurations tend to overestimate rainfall at lower thresholds (below 3 mm/h) and at higher extremes (above 10 mm/h), while moderate rainfall shows less bias. At the extremes, both simulations behave similarly; however, CP-ON better matches moderate rainfall values, whereas CP-OFF aligns more closely with the observation at light rainfall values.

This analysis is further supported by Figure 5.25 B. The horizontal line represents a 50% frequency (i.e., the median of the distribution). This figure suggests that CP-ON produces a higher average rainfall compared to the other simulations, with CP-OFF showing the closest alignment with GPM-IMERG, and ERA5 producing the lowest values. This behavior is consistent with the cloud morphology analysis, which indicated that CP-ON tends to generate deeper clouds and, consequently, more precipitation. Additionally, for a higher percentage of the sample, near 90%, CP-ON most closely follows the GPM-IMERG curve, reinforcing its better performance in simulating moderate to heavy rainfall.

Looking at the other sensitivity experiments involving the cold pool parametrization, a similar trend is observed (Figure 5.25, C and E). Overall, the parametrization improves the distribution of moderate rainfall, particularly when it is active.

The most significant differences appear in Figure 5.25 D and F. In Figure 5.25 D, an improvement in rainfall distribution is evident with increased horizontal resolution (CP-15km), which more closely reproduces the observed GPM-IMERG distribution across all thresholds. It also presents the most accurate average rainfall among all MONAN experiments. On the other hand, panel F demonstrates that certain parameter changes within the cold pool parametrization can degrade the representation of mean rainfall distribution. For example, CP-3H and CP-D025 curves deviate most significantly from the GPM-IMERG mean.

These results suggest that further sensitivity testing, preferably using ensemble approaches, could help better calibrate the forecasted rainfall distributions. Future studies should also include additional hurricane cases to define an optimal cold pool parametrization applicable to various ocean basins.

Finally, one should note that for heavy rainfall thresholds, the curves become indistinguishable, so for the next section we will show a closer look into these thresholds.

### 5.2.3.3 Rainfall extremes

The following panels represent the CDFs computed for data frequencies above 85% of each sample (forecasts and datasets), where panels B, D, and F are derived from Figure 5.25. In these plots, the vertical purple line indicates the threshold value on the x-axis corresponding to a frequency of 95%. For GPM-IMERG, this point corresponds to a threshold of 5.5 mm/h, meaning that 95% of GPM-IMERG data values are equal to or below 5.5 mm/h. On the right side of each graph, the corresponding frequency values for each dataset at this 5.5 mm/h threshold are provided. For example, 98.8% of ERA5 data exhibit rainfall rates equal to or below 5.5 mm/h; thus, only 1.2% of ERA5 data exceed this threshold (compared to 5% from the GPM-IMERG observation).

Following this logic, the proportion of heavy rainfall produced by each sample becomes clear. CP-ON exhibits the highest heavy rainfall proportion, with approximately 5.2%, whereas CP-OFF shows only 3.3%. Additionally, it is worth noting that the percentage of extreme rainfall observed by GSMAp is relatively small, at just 3%.

Among the sensitivity experiments, the percentage is similar across configurations, with CP-1HD050 yielding 94.2% of values below 5.5 mm/h (Figure 5.26 D), followed by CP-1H and CP-D025 with 94.1% (Figure 5.26 F).

Furthermore, Figure 5.27 presents a set of CDFs panels computed using the same spatial and temporal domain as in Figure 5.25. That is, each CDF is calculated for the area (latitude and longitude) corresponding to Figure 5.25 and at specific time steps, displayed in panels A (July 4th 00 UTC), B (July 5th 16 UTC), and C (July 7th 10 UTC). The purpose is to examine how the rainfall distribution behaves when focusing more closely on the hurricane's vicinity.

In the first column (A), corresponding to the moment Beryl reaches its maximum precipitation according to official reports, rainfall is overestimated by the experiments employing the cold pool parameterization, with CP-15km being the closest to the reference. CP-OFF overestimates light rainfall thresholds and significantly overestimates the heavy rainfall range.

After Beryl passes over the Yucatán Peninsula (panel B), most forecasts and datasets tend to overestimate rainfall overall, but they converge better around the heavier rainfall thresholds.

Upon landfall in Texas (panel C), when Beryl re-intensifies to a Category 1 hurricane, there is again a trend of overestimated rainfall. However, this trend is not mirrored by all datasets, and some experiments, such as CP-15km, CP-OFF, and CP-1HD050, show closer agreement at moderate rainfall thresholds.

#### **5.2.3.4 MONAN performance at forecasting rainfall**

As this chapter presents a large number of figures and maps, this section aims to concisely summarize the main results by focusing specifically on the eyeball comparison between MONAN and ERA5.

In terms of the Equitable Threat Score (ETS), MONAN shows similar performance to ERA5 overall. The most notable differences occur in the moderate rainfall thresholds, where ERA5 performs higher ETS values.

The Pearson correlation coefficient in the accumulated scene for MONAN averaged 0.45, which is generally considered a moderate correlation, in contrast with ERA5's value of 0.69, which indicates a strong correlation. It is important to highlight that MONAN's correlation deteriorates substantially with increasing forecast lead time. This suggests that if MONAN were initialized more frequently (e.g., with updated initial conditions every day), its correlation values might approach those of ERA5. Despite this degradation, the spatial distribution of extreme rainfall areas is broadly consistent between MONAN and ERA5.

Notably, MONAN can reproduce the convective structures observed by satellite, even with its 30 km horizontal resolution, something that ERA5 fails to capture in certain cases, such as the spiral-shaped rainbands (see case Figure X.X.X).

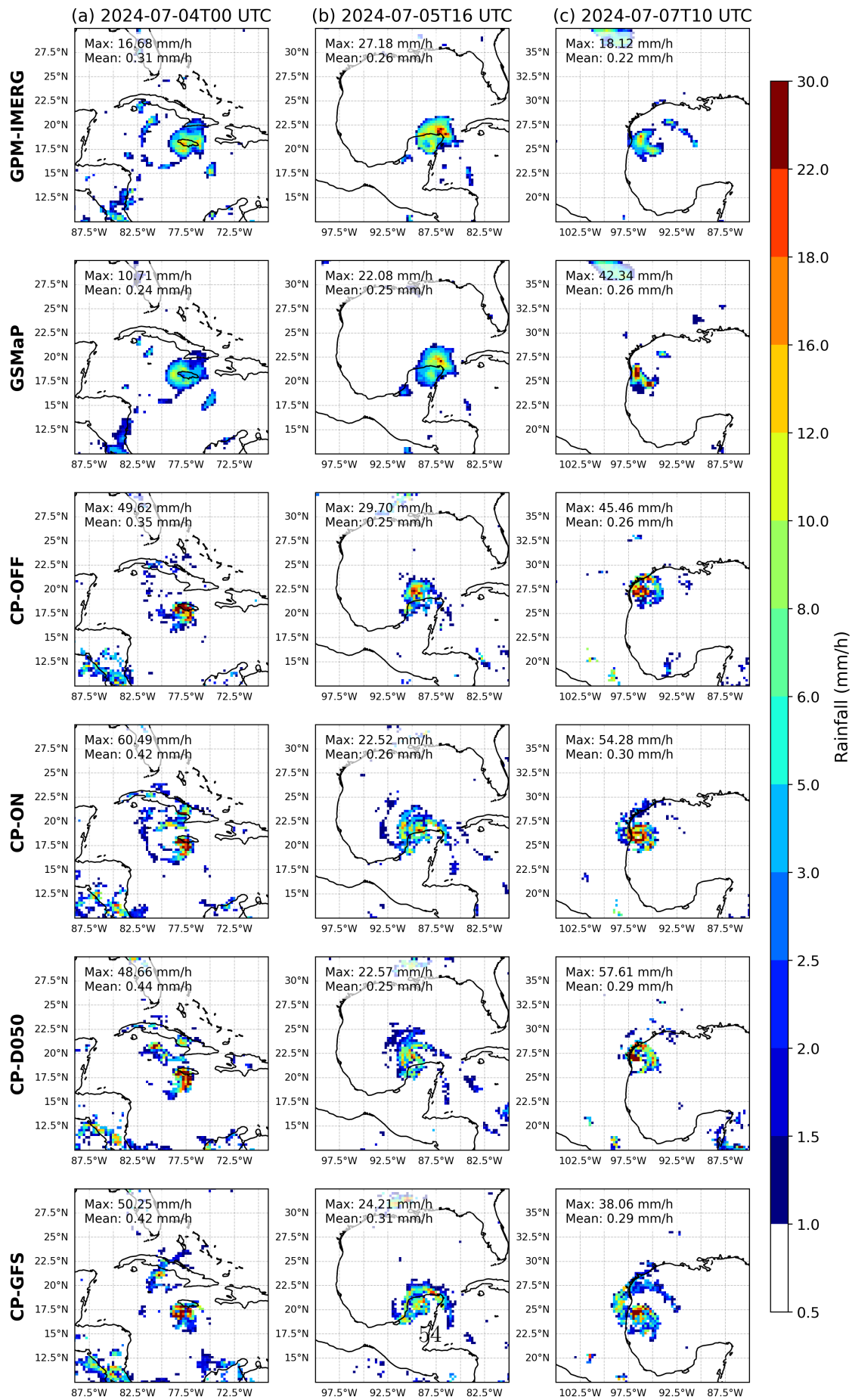
When analyzing the rainfall distribution and mean values, it was observed that MONAN tends to underestimate rainfall at both lower and higher thresholds, while ERA5 tends to overestimate rainfall at moderate and extreme thresholds. Besides, the mean rainfall in MONAN is slightly overestimated, but on the other hand, in ERA5, it is consistently overestimated.

Finally, in terms of extreme rainfall prediction, MONAN forecasts are closer to the GPM-IMERG reference data, particularly when the convective parameterization is enabled. ERA5, however, tends to significantly overestimate rainfall extremes: for example, 2% of the sample with extreme rainfall, compared to 5% observed in GPM-IMERG.

#### **5.2.4 Discussion of key outcomes**

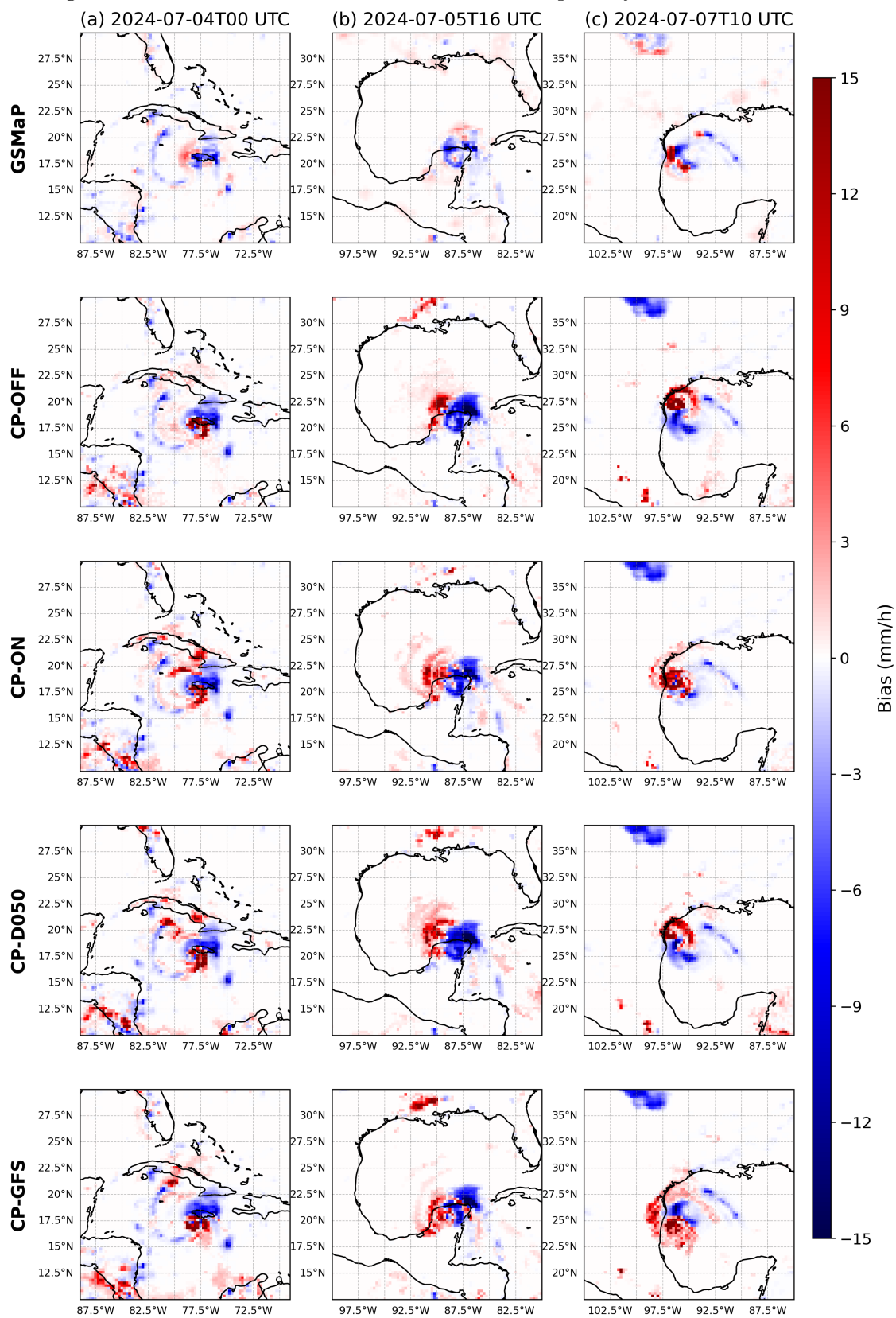
a fazer, dale bianca

Figure 5.20 - Selected snapshots of rainfall fields from IMERG and GSMAp (30 km resolution) for key time steps



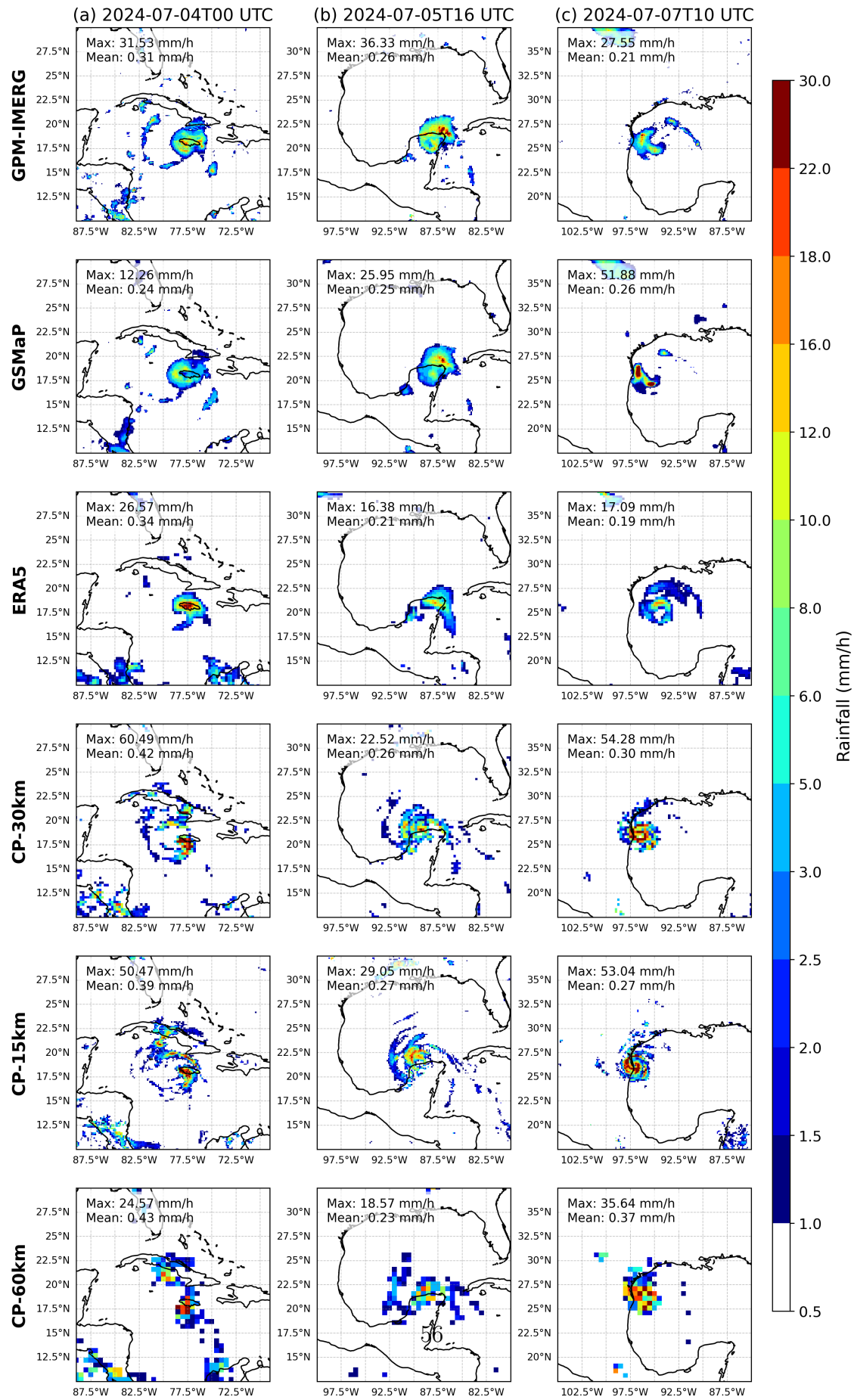
Source: Made by the author (2025).

Figure 5.21 - Bias relative to GPM-IMERG for tropical cyclone rainfall forecasts



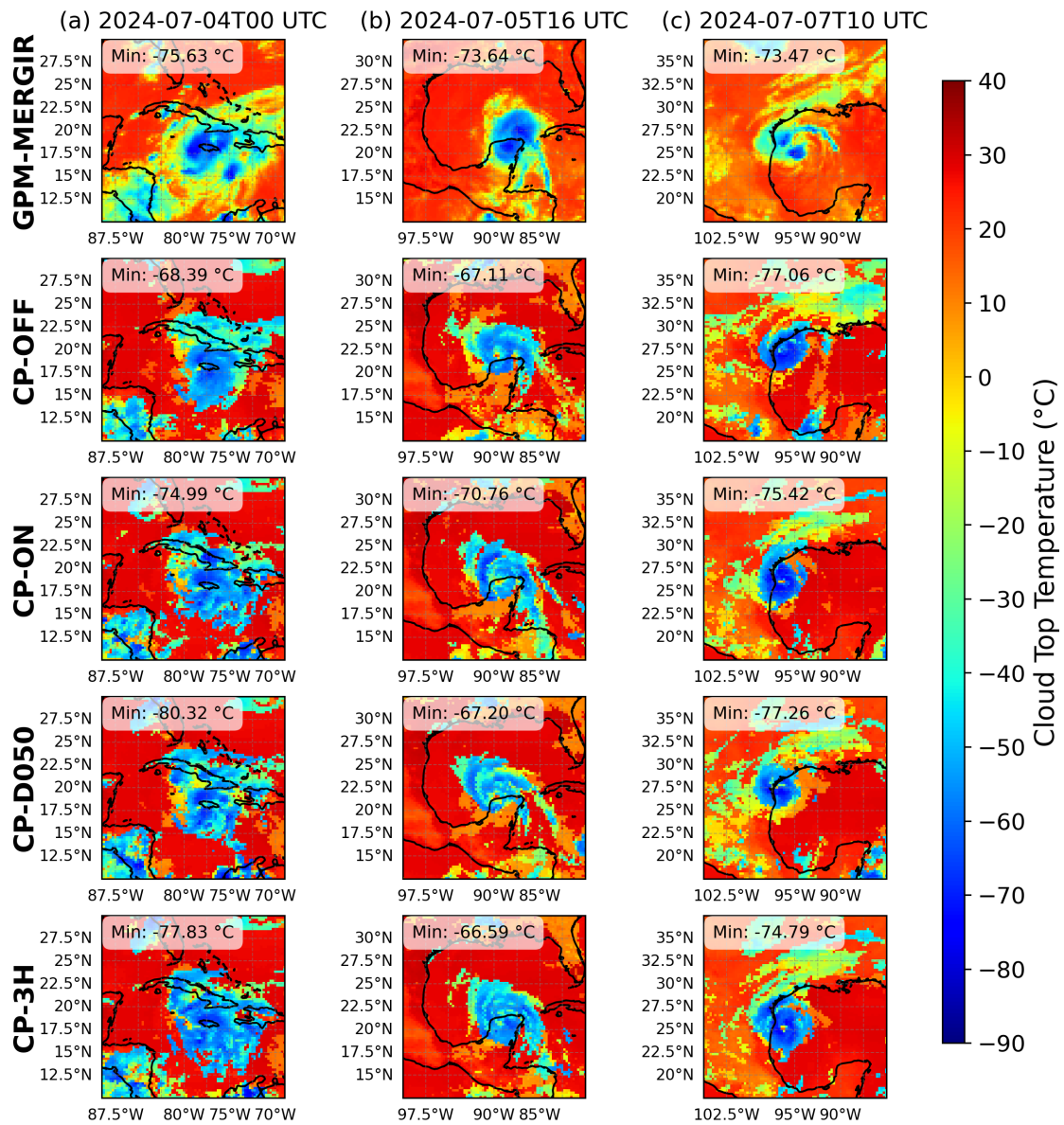
Source: Made by the author (2025).

Figure 5.22 - Spatial bias relative to GPM-IMERG, highlighting displacement effects in tropical cyclone forecasts



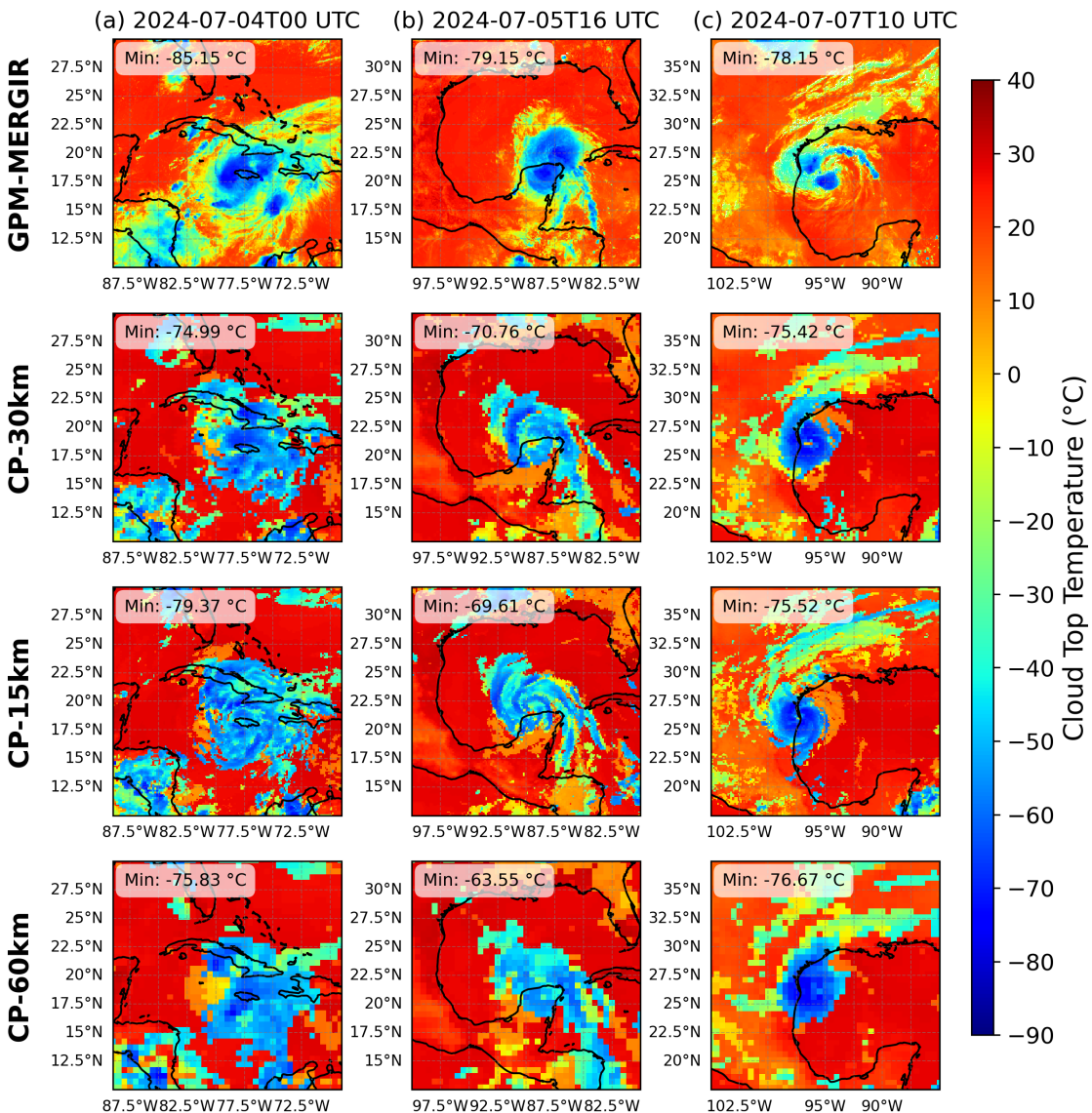
Source: Made by the author (2025).

Figure 5.23 - Cloud-top brightness temperature snapshots for assessing cloud morphology and vertical structures



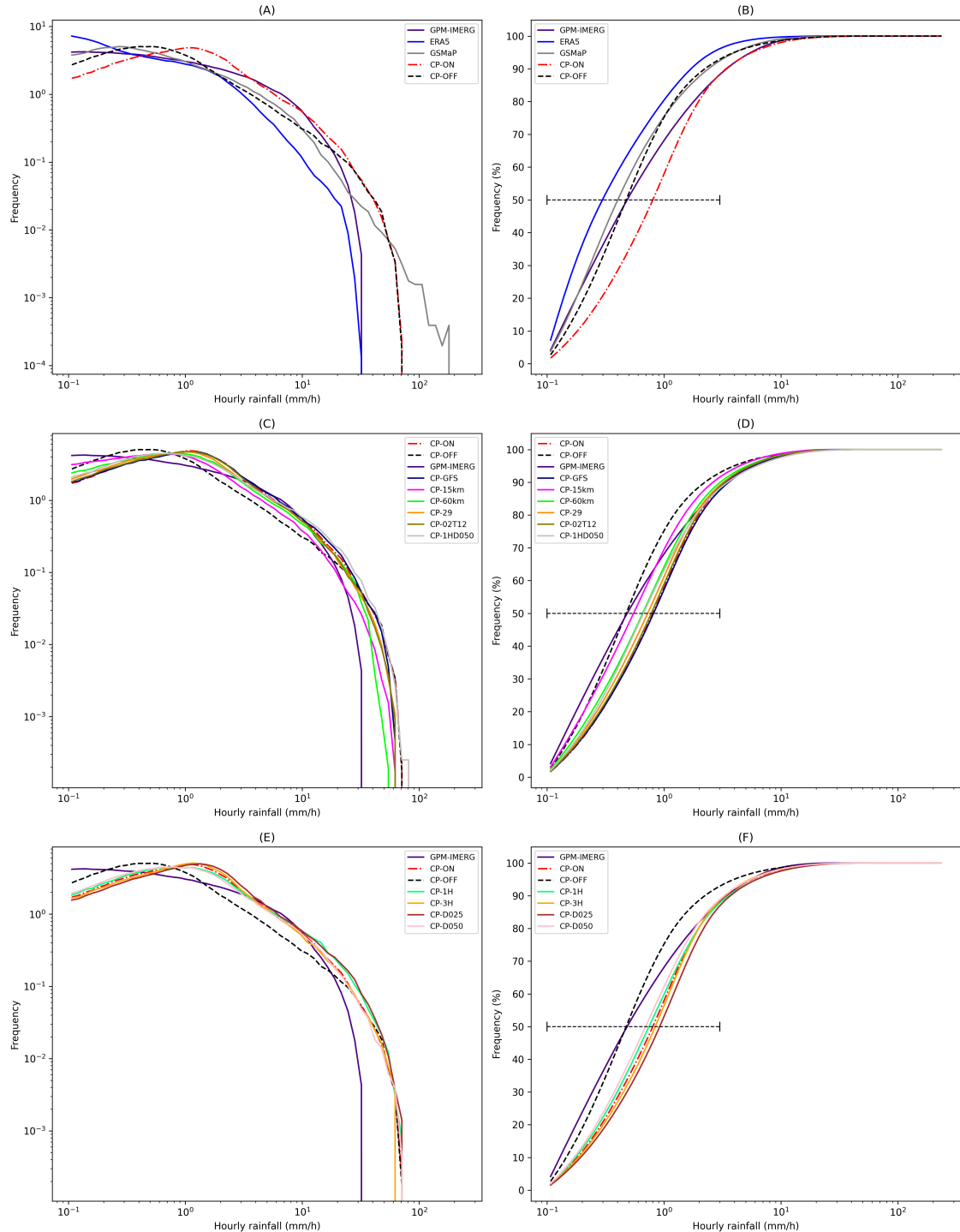
Source: Made by the author (2025).

Figure 5.24 - Effect of horizontal resolution on cloud-top brightness temperature fields



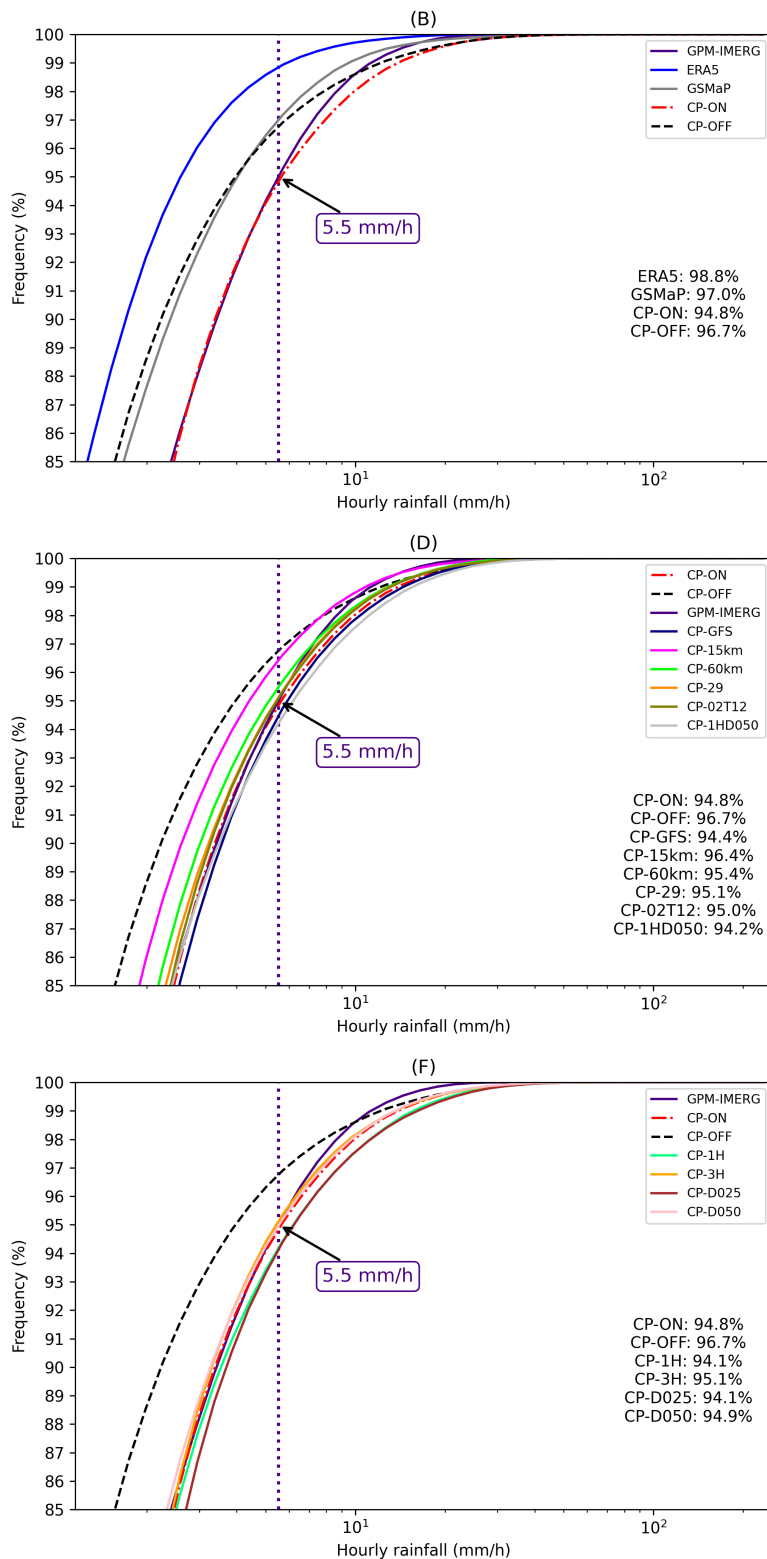
Source: Made by the author (2025).

Figure 5.25 - Probability density (left) and cumulative distribution functions (right) of hourly rainfall for each experiment and reference dataset



Source: Made by the author (2025).

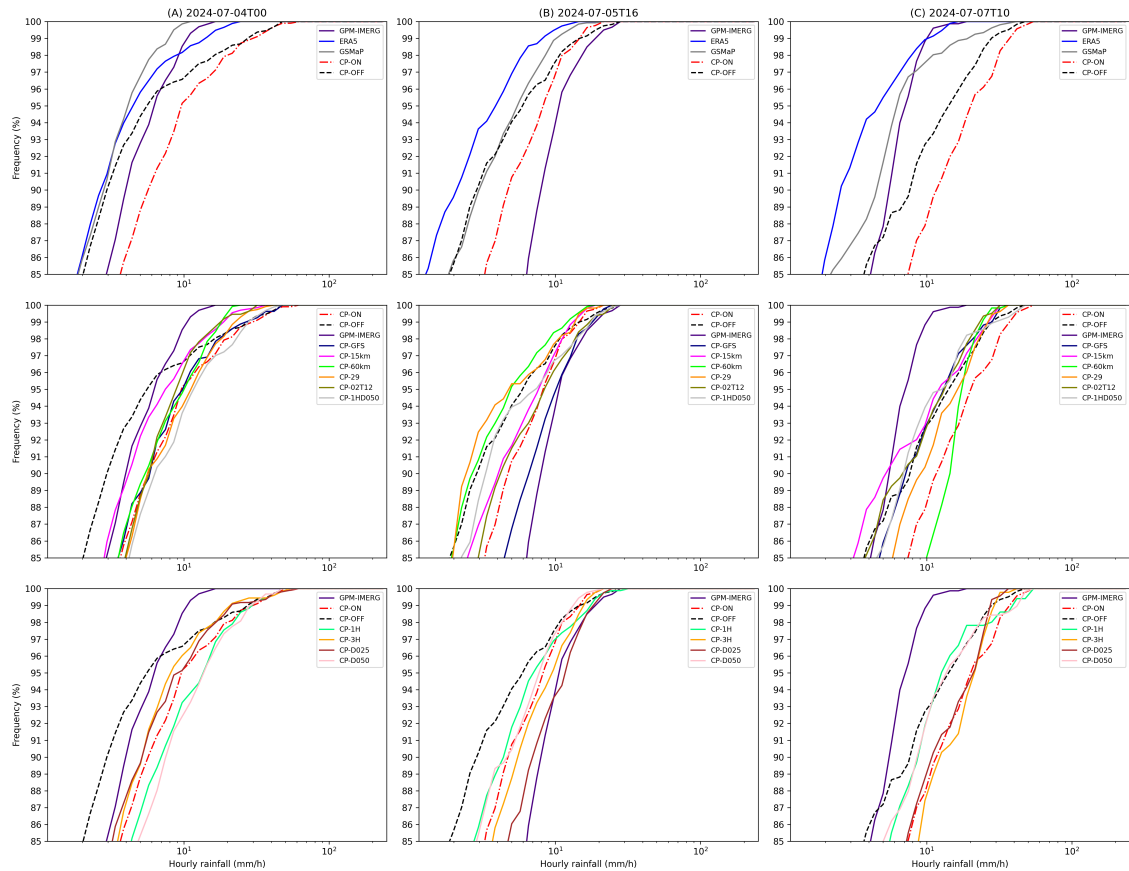
Figure 5.26 - CDFs above the 85th percentile of hourly rainfall, with 95% threshold comparison across datasets



Source: Made by the

author (2025).

Figure 5.27 - CDFs of hourly rainfall at selected time steps within the hurricane domain



Source: Made by the author (2025).



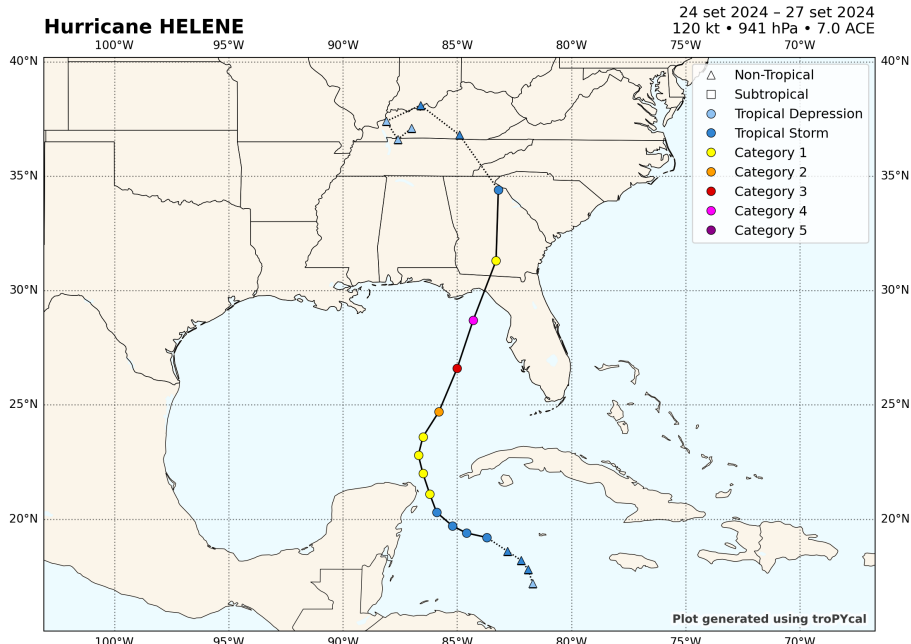
## 6 CASE STUDY: HURRICANE HELENE – TESTING THE IMPROVED PARAMETRIZATION

This chapter examines the results of the optimal configuration of the cold pool parameterization parameters, the impact of the parameterization itself, and an increase in horizontal resolution during another North Atlantic Basin hurricane season in 2024: Helene. The storm occurred between September 24 and September 27. As in previous analyses, we begin with a description of the event, followed by results categorized into three main features: trajectory, intensity, and rainfall, under the workflow outlined in section 4. By the end of the section, we will discuss the findings in detail.

### 6.1 Event description - Helene

Hurricane Helene was a destructive and rapidly intensifying tropical cyclone that hugely impacted the southeastern United States in late September 2024. Originating in the Central American Gyre (western Caribbean), Helene was first classified as a tropical storm at 0600 UTC on 25 September, approximately 50 nautical miles east of Cozumel, Mexico. Figure 6.1 show the best track trajectory made by the hurricane.

Figure 6.1 - Best track trajectory of Hurricane Helene (September 2024)



Source: Made by the author (2025).

By 1200 UTC the same day (25 September), Helene steadily strengthened in conducive environmental conditions of low wind shear, high moisture, and very warm sea surface temperatures, intensifying into a hurricane just east of Cancún by 1800 UTC. It later entered the Gulf of Mexico as a category 1 system on the Saffir-Simpson Hurricane Wind Scale.

Helene's intensification was notably rapid, surpassing the threshold for rapid intensification (>35 mph increase in wind speed in 24 hours ([National Hurricane Center, 2024a](#))). Just six hours later, it reached its peak intensity as a category 4 hurricane, with sustained winds of 120 kt (140 mph), approximately 80 nautical miles south-southwest of the Florida Big Bend region.

The first landfall occurred near Perry, Florida, at approximately 0310 UTC on 27 September. At the time, Helene maintained its category 4 status and was moving rapidly north-northeastward. The storm brought catastrophic storm surge to coastal communities, with inundation levels reaching 12 to 16 feet (3.7 - 4.9 meters) above ground level in the Big Bend region, particularly devastating Keaton Beach and Steinhatchee. Additional surge heights of 6 to 8 feet (1.8 - 2.4 meters) were observed as far south as Tampa ([CENTER, 2024](#)).

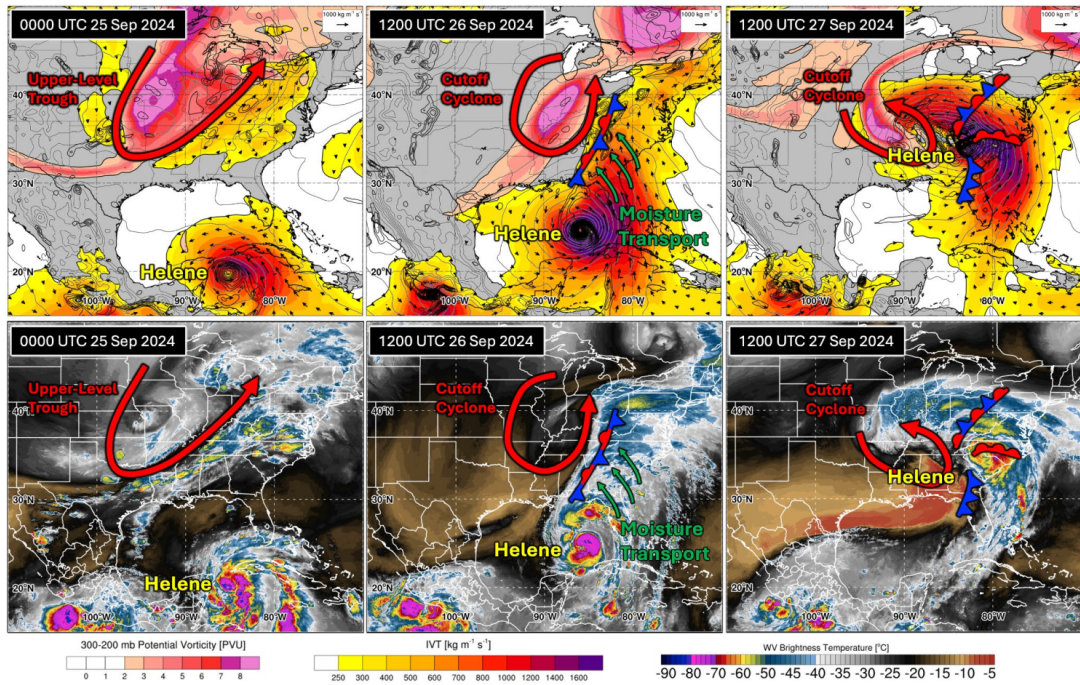
As Helene moved inland on the morning of 27 September, it gradually weakened due to land interaction. By 0900 UTC, the system had been downgraded to a tropical storm while located near Macon, Georgia. Despite the weakening, Helene's impacts intensified as the storm interacted with a stationary frontal boundary stretching from the central Gulf Coast to the southern Appalachians. Enhanced low-level convergence and orographic lift contributed to excessive rainfall, particularly in these mountainous regions. Figure 6.4 pictures this large-scale interaction.

Helene's moisture-laden circulation delivered extreme precipitation across a broad swath of the southeastern United States. The heaviest observed rainfall total was recorded in Busick, North Carolina, where 30.78 inches (approximately 782 mm) fell between 25 and 28 September. The orographic influence was particularly evident in areas such as Georgia and western North Carolina, where intense rainfall led to flash flooding, river overflow, and landslides. A satellite image in Figure XXX shows Helene and the large tail of convection when passing thought North Carolina.

The small mountain town of Chimney Rock, NC, was among the hardest hit, with flood-waters destroying much of the local infrastructure ([Encyclopaedia Britannica, Inc., 2025](#)). Table 6.1 summarizes the total rainfall by state.

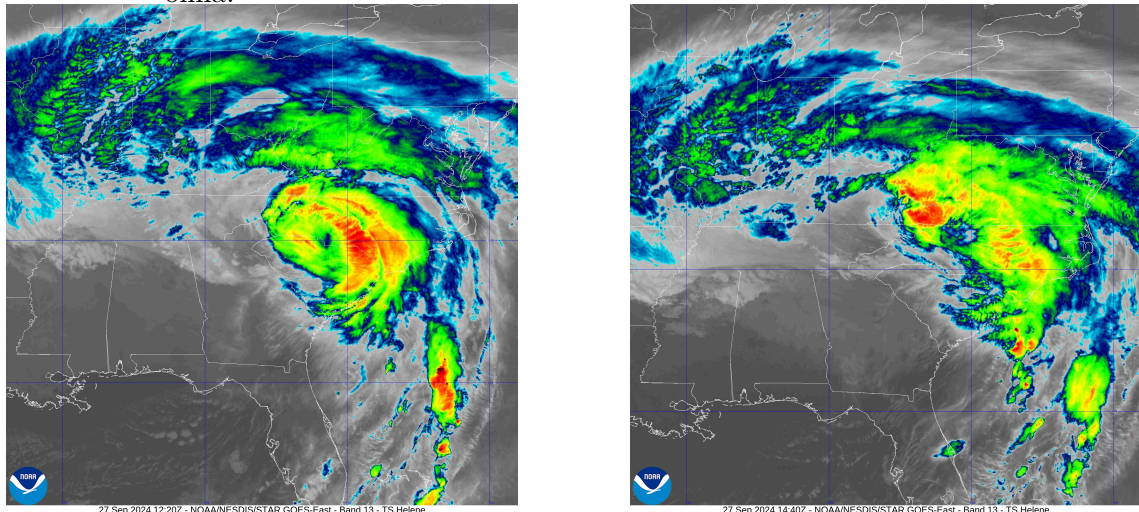
By 1800 UTC on 27 September, Helene had become post-tropical as it merged with a mid-

Figure 6.2 - Synoptic-scale interaction between Hurricane Helene and a stationary frontal boundary over the southeastern U.S



Source: (National Hurricane Center, 2024b).

Figure 6.3 - Satellite images of Hurricane Helene with trailing convection over North Carolina.



Source:.

latitude cutoff low over the Tennessee Valley and transitioned into an extratropical cyclone over southern Kentucky. The remnant low persisted until 28 September, performing a slow

Table 6.1 - Highest Rainfall Totals by State

<b>State</b>	<b>County</b>	<b>Location</b>	<b>Rainfall (inches)</b>
North Carolina	Yancey	Busick	30.78
South Carolina	Greenville	Sunfish Mountain	21.66
Georgia	Rabun	3.5 mi NE Dillard	14.64
Florida	Liberty	Sumatra	14.39
Tennessee	Johnson	Trade	10.98
Virginia	Grayson	5.3 mi SW Galax	10.89
Ohio	Scioto	Rosemount	8.51
Alabama	Houston	1.6 mi NNE Pansey	8.50
Kentucky	Henderson	Henderson	7.67
Illinois	Massac	Ft. Massac St. Park	7.47
West Virginia	Mercer	Bluefield	6.11
Indiana	Clark	2.6 mi E Henryville	5.69

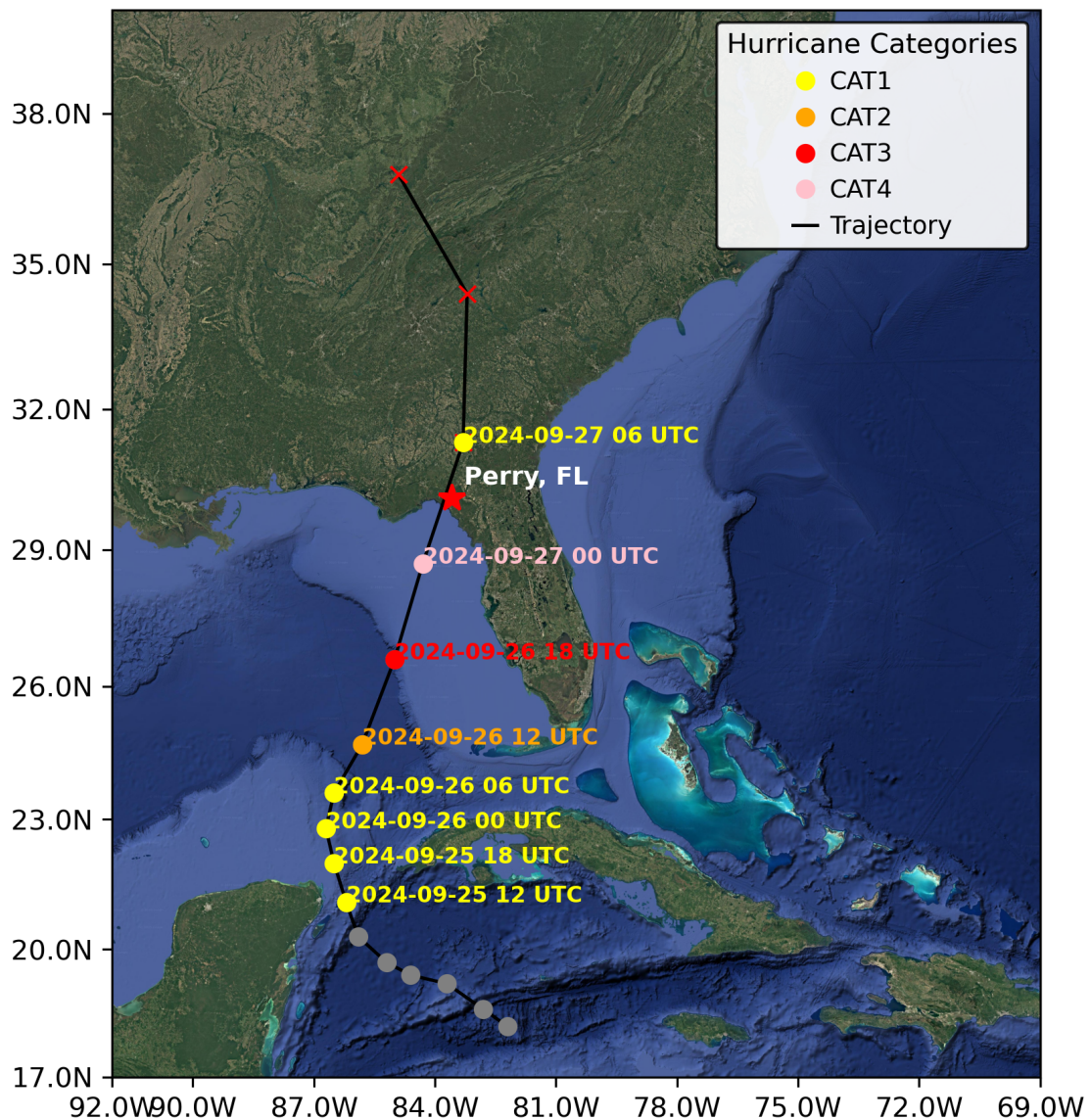
Source: ([National Hurricane Center, 2024b](#)).

cyclonic loop before dissipating over north-central Tennessee.

Hurricane Helene resulted in widespread devastation across Florida, Georgia, the Carolinas, and Tennessee. Approximately 4 million people lost power due to infrastructure damage. With at least 250 reported fatalities, 176 of which were direct, Helene became the deadliest hurricane in the contiguous United States since Hurricane Katrina in 2005.

For our simulations, we compute the entire period from 24 12UTC September to 27. Following figure XXX, the trajectory in the period of our simulations is represented by....

Figure 6.4 - Criar um titulo aqui



Source: .

## **6.2 Results and analysis of hurricane Helene**

### **6.2.1 Trajectory**

### **6.2.2 Intensity**

### **6.2.3 Rainfall**

#### **6.2.3.1 Pattern and spatial rainfall distribution**

#### **6.2.3.2 Rainfall mean and overall distribution**

#### **6.2.3.3 MONAN performance at forecasting rainfall**

### **6.3 Discussion of key outcomes**

## **7 CONCLUSIONS AND FUTURE WORK**

### **7.1 Future Work**



## A APPENDIX - THE MASS FLUX DEDUCTION

Here is briefly described the mass flux approach in the cold pool parameterization context.



## A APPENDIX B - THE TRACKING ALGORITHM

Descrever o algoritmo assim como referencias.



## REFERENCES

- BAGTASA, G. Assessment of tropical cyclone rainfall from gsmap and gpm products and their application to analog forecasting in the philippines. **Atmosphere**, MDPI, v. 13, n. 9, p. 1398, 2022. 9
- BOPAPE, M.-J. M.; CARDOSO, H.; PLANT, R. S.; PHADULI, E.; CHIKOORE, H.; NDARANA, T.; KHALAU, L.; RAKATE, E. Sensitivity of tropical cyclone idai simulations to cumulus parametrization schemes. **Atmosphere**, MDPI, v. 12, n. 8, p. 932, 2021. 5
- BRACKINS, J. T.; KALYANAPU, A. J. Evaluation of parametric precipitation models in reproducing tropical cyclone rainfall patterns. **Journal of Hydrology**, Elsevier, v. 580, p. 124255, 2020. 44
- CENTER, F. S. U. C. **Hurricane Helene Summary Report**. 2024. Accessed: 2025-05-24. Disponível em: <<https://climatecenter.fsu.edu/images/docs/Hurricane-Helene-Summary-Report.pdf>>. 64
- DEMARIA, M.; KNAFF, J.; SAMPSON, C. Evaluation of long-term trends in tropical cyclone intensity forecasts. **Meteorology and Atmospheric Physics**, Springer, v. 97, n. 1, p. 19–28, 2007. 17
- DITCHEK, S. D.; SIPPEL, J. A.; MARINESCU, P. J.; JR, G. J. A. Improving best track verification of tropical cyclones: A new metric to identify forecast consistency. **Weather and Forecasting**, v. 38, n. 6, p. 817–831, 2023. 15
- DONKIN, P. T.; ABIODUN, B. J. Capability and sensitivity of mpas-a in simulating tropical cyclones over the south-west indian ocean. **Modeling Earth Systems and Environment**, Springer, v. 9, n. 1, p. 527–542, 2023. 36
- DULAC, W.; CATTIAUX, J.; CHAUVIN, F.; BOURDIN, S.; FROMANG, S. Assessing the representation of tropical cyclones in era5 with the cnrm tracker. **Climate Dynamics**, Springer, v. 62, n. 1, p. 223–238, 2024. 5, 6, 41
- Encyclopaedia Britannica, Inc. **Hurricane Helene**. 2025. <<https://www.britannica.com/event/Hurricane-Helene>>. Accessed: 2025-05-24. 64
- FENG, Z.; HAGOS, S.; ROWE, A. K.; BURLEYSON, C. D.; MARTINI, M. N.; SZOEKE, S. P. de. Mechanisms of convective cloud organization by cold pools over tropical warm ocean during the amie/dynamo field campaign. **Journal of Advances in Modeling Earth Systems**, Wiley Online Library, v. 7, n. 2, p. 357–381, 2015. 49
- FREITAS, S. R.; GRELL, G. A.; CHOVERT, A. D.; DIAS, M. A. F. S.; NASCIMENTO, E. de L. A parameterization for cloud organization and propagation by evaporation-driven cold pool edges. **Journal of Advances in Modeling Earth Systems**, Wiley Online Library, v. 16, n. 1, p. e2023MS003982, 2024. 1, 10, 49
- FREITAS, S. R.; GRELL, G. A.; MOLOD, A.; THOMPSON, M. A.; PUTMAN, W. M.; SILVA, C. M. Santos e; SOUZA, E. P. Assessing the grell-freitas convection parameterization in the nasa geos modeling system. **Journal of Advances in Modeling Earth Systems**, Wiley Online Library, v. 10, n. 6, p. 1266–1289, 2018. 10

- GAO, K.; HARRIS, L.; BENDER, M.; CHEN, J.-H.; ZHOU, L.; KNUTSON, T. Regulating fine-scale resolved convection in high-resolution models for better hurricane track prediction. **Geophysical Research Letters**, Wiley Online Library, v. 50, n. 13, p. e2023GL103329, 2023. 16
- GRELL, G. A.; FREITAS, S. R. A scale and aerosol aware stochastic convective parameterization for weather and air quality modeling. **Atmospheric Chemistry and Physics**, Copernicus GmbH, v. 14, n. 10, p. 5233–5250, 2014. 10
- GUNASEKERA, R.; ESCUDERO, O. A. I.; DANIELL, J. E.; POMONIS, A.; STONE, H.; TOYOS, G. P.; BRAND, J.; HERNANDEZ, R. A. R.; CUBAS, D.; WEIL, J. R. Global rapid post-disaster damage estimation (grade) report: Hurricane beryl 2024-saint vincent and the grenadines: Report as of july 26, 2024. < bound method Organization. get\_name\_with\_acronym of< Organization: World . . . , 2024. 25
- HAERTER, J. O.; BÖING, S. J.; HENNEBERG, O.; NISSEN, S. B. Reconciling cold pool dynamics with convective self-organization. **arXiv preprint arXiv:1810.05518**, 2018. 49
- HEMING, J. Tropical cyclone tracking and verification techniques for met office numerical weather prediction models. **Meteorological Applications**, Wiley Online Library, v. 24, n. 1, p. 1–8, 2017. 17
- HERSBACH, H.; BELL, B.; BERRISFORD, P.; HIRAHARA, S.; HORÁNYI, A.; MUÑOZ-SABATER, J.; NICOLAS, J.; PEUBEY, C.; RADU, R.; SCHEPERS, D. et al. The era5 global reanalysis. **Quarterly journal of the royal meteorological society**, Wiley Online Library, v. 146, n. 730, p. 1999–2049, 2020. 5
- HONG, S.-Y.; LIM, J.-O. J. The wrf single-moment 6-class microphysics scheme (wsm6). **Asia-Pacific Journal of Atmospheric Sciences**, v. 42, n. 2, p. 129–151, 2006. 10
- HUFFMAN, G. Gpm imerg final precipitation l3 half hourly 0.1 degree× 0.1 degree v06. (**No Title**), 2019. 7
- IACONO, M. J.; DELAMERE, J. S.; MLAWER, E. J.; SHEPHARD, M. W.; CLOUGH, S. A.; COLLINS, W. D. Radiative forcing by long-lived greenhouse gases: Calculations with the aer radiative transfer models. **Journal of Geophysical Research: Atmospheres**, Wiley Online Library, v. 113, n. D13, 2008. 10
- JANOWIAK, J.; JOYCE, B.; XIE, P. **NCEP/CPC L3 half hourly 4 km global (60S–60N) merged IR V1. Goddard Earth Sciences Data and Information Services Center (GES DISC)**. 2017. 8
- KNAPP, K. R.; KRUK, M. C.; LEVINSON, D. H.; DIAMOND, H. J.; NEUMANN, C. J. The international best track archive for climate stewardship (ibtracs) unifying tropical cyclone data. **Bulletin of the American Meteorological Society**, American Meteorological Society, v. 91, n. 3, p. 363–376, 2010. 5
- LANDSEA, C. W.; FRANKLIN, J. L. Atlantic hurricane database uncertainty and presentation of a new database format. **Monthly Weather Review**, v. 141, n. 10, p. 3576–3592, 2013. 17
- LI, Z.; TAN, Z.-M.; BAI, L. Generative deep learning reconstructs tropical cyclone microwave data from geostationary infrared radiometers. **Authorea Preprints**, Authorea, 2025. 27, 28, 44

LUITEL, B.; VILLARINI, G.; VECCHI, G. A. Verification of the skill of numerical weather prediction models in forecasting rainfall from us landfalling tropical cyclones. **Journal of hydrology**, Elsevier, v. 556, p. 1026–1037, 2018. 44

MARCHOK, T.; ROGERS, R.; TULEYA, R. Validation schemes for tropical cyclone quantitative precipitation forecasts: Evaluation of operational models for us landfalling cases. **Weather and forecasting**, v. 22, n. 4, p. 726–746, 2007. 18, 19, 44

MAY, J.; HARANDI, M.; TYO, J. S.; HU, L.; RITCHIE-TYO, E. A. A cnn system for segmenting tropical cyclones neighborhoods in geostationary images. In: IEEE. **IGARSS 2024-2024 IEEE International Geoscience and Remote Sensing Symposium**. [S.l.], 2024. p. 8259–8262. 5

MESINGER, F. Bias adjusted precipitation threat scores. **Advances in Geosciences**, Copernicus Publications Göttingen, Germany, v. 16, p. 137–142, 2008. 18

Met Office. **Observed and forecast tracks: northern hemisphere 2024**. 2024. Accessed: 2025-05-24. Disponível em: <<https://www.metoffice.gov.uk/research/weather/tropical-cyclones/verification/seasons/nhem2024>>. 39

MITCHELL, K. The community noah land-surface model (lsm). **User's Guide public release version**, v. 2, n. 1, p. 3660–3667, 2005. 10

MOON, J.; PARK, J.; CHA, D.-H.; MOON, Y. Five-day track forecast skills of wrf model for the western north pacific tropical cyclones. **Weather and Forecasting**, v. 36, n. 4, p. 1491–1503, 2021. 15

NAKANISHI, M.; NIINO, H. Development of an improved turbulence closure model for the atmospheric boundary layer. **Journal of the Meteorological Society of Japan. Ser. II**, Meteorological Society of Japan, v. 87, n. 5, p. 895–912, 2009. 10

National Hurricane Center. **Hurricane Helene Advisory Number 9**. 2024. Accessed: 2025-05-24. Disponível em:  
<[https://www.nhc.noaa.gov/archive/2024/helene/helene\\_advisory\\_09.pdf](https://www.nhc.noaa.gov/archive/2024/helene/helene_advisory_09.pdf)>. 64

\_\_\_\_\_. **Tropical Cyclone Report: Hurricane Helene (AL092024)**. [s.n.], 2024. Acesso em: 24 maio 2025. Disponível em:  
<[https://www.nhc.noaa.gov/data/tcr/AL092024\\_Helene.pdf](https://www.nhc.noaa.gov/data/tcr/AL092024_Helene.pdf)>. 65, 66

NYONGESA, A. M.; SHI, D.; LI, S.; LI, Q. Influence of convective parameterization on the simulation of tropical cyclones over the south west indian ocean: A case study of tropical cyclone idai (2019). **Atmospheric Research**, Elsevier, v. 306, p. 107461, 2024. 15

REDDY, M. V.; MITRA, A. K.; MOMIN, I.; KRISHNA, U. M. How accurately satellite precipitation products capture the tropical cyclone rainfall? **Journal of the Indian Society of Remote Sensing**, Springer, v. 50, n. 10, p. 1871–1884, 2022. 9

SAKAEDA, N.; TORRI, G. The observed effects of cold pools on convection triggering and organization during dynamo/amie. **Journal of Geophysical Research: Atmospheres**, Wiley Online Library, v. 128, n. 17, p. e2023JD038635, 2023. 49

SHEPHERD, T. J.; WALSH, K. J. Sensitivity of hurricane track to cumulus parameterization schemes in the wrf model for three intense tropical cyclones: Impact of convective asymmetry. **Meteorology and Atmospheric Physics**, Springer, v. 129, p. 345–374, 2017. 17

SIPPEL, J. A.; WU, X.; DITCHEK, S. D.; TALLAPRAGADA, V.; KLEIST, D. T. Impacts of assimilating additional reconnaissance data on operational gfs tropical cyclone forecasts. **Weather and Forecasting**, v. 37, n. 9, p. 1615–1639, 2022. 38

SKAMAROCK, W. C.; KLEMP, J. B.; DUDA, M. G.; FOWLER, L. D.; PARK, S.-H.; RINGLER, T. D. A multiscale nonhydrostatic atmospheric model using centroidal voronoi tesselations and c-grid staggering. **Monthly Weather Review**, v. 140, n. 9, p. 3090–3105, 2012. 11

VOGEL, R.; KONOW, H.; SCHULZ, H.; ZUIDEMA, P. A climatology of trade-wind cumulus cold pools and their link to mesoscale cloud organization. **Atmospheric Chemistry and Physics**, Copernicus Publications Göttingen, Germany, v. 21, n. 21, p. 16609–16630, 2021. 49

YANG, S.; SURRETT, M.; WHITCOMB, T. R.; CAMACHO, C. Evaluation of imerg and gsmap for tropical cyclone applications. **Geophysical Research Letters**, Wiley Online Library, v. 51, n. 4, p. e2023GL106414, 2024. 5, 9

ZHOU, F.; TOTH, Z. On the prospects for improved tropical cyclone track forecasts. **Bulletin of the American Meteorological Society**, v. 101, n. 12, p. E2058–E2077, 2020. 38

ZHOU, Y.; MATYAS, C. J. Regionalization of precipitation associated with tropical cyclones using spatial metrics and satellite precipitation. **GIScience & Remote Sensing**, Taylor & Francis, v. 58, n. 4, p. 542–561, 2021. 5